Journal of Alloys and Compounds 1040 (2025) 183431

Contents lists available at ScienceDirect

Journal of Alloys and Compounds

journal homepage: www.elsevier.com/locate/jalcom

Effect of nickel on the mechanical properties of spray-formed Al-15Si-2Cu alloy at elevated temperatures

Dayanand M. Goudar [a], Mehabubsubahani R. Alavandi [a], Subraya Krishna Bhat [b,*], Raghukumar Bommenahalli [c], Rajashekar V. Kurahatti [d], Deesy G. Pinto [e], K. Raju [f,*]

[a] Department of Mechanical Engineering, Tontadarya College of Engineering, Gadag 582101, India
[b] Department of Mechanical and Industrial Engineering, Manipal Institute of Technology, Manipal Academy of Higher Education, Manipal 576104, India
[c] Dekra Certification Inc, California, USA
[d] Department of Mechanical Engineering, Basaveshwar Engineering College, Bagalkot 587101, India
[e] Department of Civil Engineering and Architecture, University of Beira Interior, Calçada Fonte do Lameiro 6, Covilhã 6200-358, Portugal
[f] Department of Mechanical Engineering, St. Joseph Engineering College, Mangaluru 575028, India

ARTICLE INFO

Keywords:
As-cast alloy
Spray formed alloy
Microstructure
Hardness
Tensile strength

ABSTRACT

In the present study, the effect of nickel (Ni) on the mechanical properties of spray-formed (SF) Al-15Si-2Cu alloy at different temperatures was examined and evaluated with that of the as-cast (AC) alloy. The microstructure of SF alloys revealed uniformly distributed spherical shaped primary silicon and eutectic silicon phases along with fine Ni and Cu intermetallic particles dispersed throughout the equiaxed Al matrix. The microstructure of AC alloys consisted of coarse primary Si, flake-type eutectic phase, Cu-rich intermetallics with a complex branched morphology and a network of short strips. The mechanical properties of the alloys were assessed at temperatures of 30°C, 100°C, 200°C and 300°C. The SF alloys exhibited higher hardness than AC alloys at all temperatures with a maximum increase of 74 % at 30°C. The hardness of alloys showed a decreasing trend with increasing temperature. The mechanical strength of SF alloys was higher than that of the AC alloys across the entire temperature range from 30°C to 300°C with a decrease in ultimate tensile strength (UTS) by 4–6 % at 250°C. The SF alloys demonstrated a significant increase in UTS (25 % at 30°C and 40 % at 300°C) compared to the AC alloys. The Al-15Si-2Cu-2Ni alloy showed highest increase (14.3–18.6 %) and Al-15Si-2Cu-6Ni alloy showed the lowest increase (10.5 % to 14 %) in percent elongation between 30°C and 300°C.

1. Introduction

The automotive industry is being driven by increasingly stringent environmental regulations to develop lighter and more fuel-efficient vehicles aimed at reducing overall emissions. The Aluminum–Silicon (Al–Si) alloys are widely used in this context because of their high strength-to-weight ratio, excellent castability, superior wear resistance, and high thermal conductivity [1].

Nonetheless, the majority of Al alloys available in the market exhibit significantly reduced mechanical strength and wear behavior at temperatures above 200°C. Considerable work has been carried out in the past to modify the alloy composition and refine the microstructure to improve the high-temperature mechanical performance [2]. Multicomponent Al-Si alloys are commonly employed in the manufacturing of pistons and other critical components with an increasing demand for high-performance variants [3]. The physical and mechanical properties of these alloys are significantly influenced by the intermetallic phases including their size, morphology and distribution. Additionally, the volume fraction and distribution of the Al matrix and Si particles significantly influence the ductility, hardness and thermal expansion characteristics. Some traditional Al-Si casting alloys can meet the room-temperature requirements through the precipitation of Cu- and Mg-rich phases [4]. The addition of Cu in particular facilitates precipitation hardening by the formation of Al_2Cu intermetallics enhancing the strength and hardness under both as-cast and heat-treated conditions thereby enabling the replacement of heavier cast iron parts such as engine blocks and cylinder heads [5]. However, apart from Mg and Cu, most alloying elements exhibit limited solubility in aluminum. The

* Corresponding authors.
E-mail addresses: dmgoudar@tce.ac.in (D.M. Goudar), mralavandi.tce@gmail.com (M.R. Alavandi), sk.bhat@manipal.edu (S.K. Bhat), Raghukumar.bommenahalli@dekra.com (R. Bommenahalli), rajukurahatti@gmail.com (R.V. Kurahatti), deesy.gp.correia@ubi.pt (D.G. Pinto), rajuk@sjec.ac.in (K. Raju).

https://doi.org/10.1016/j.jallcom.2025.183431
Received 13 May 2025; Received in revised form 30 August 2025; Accepted 30 August 2025
Available online 1 September 2025

casting process often leads to equilibrium and non-equilibrium solidification paths resulting in complex intermetallic structures [6]. Elzanaty et al. [7] have assessed the mechanical properties of Al–Si–Cu alloys under high-temperature conditions and reported that the strength and hardness of the alloys increased as the Si content increased but the ductility of the alloys decreased. Gariboldi et al. [8] have found that the tensile strength in hypo-eutectic and near-eutectic Al-Si-Cu alloys declined markedly above 200°C, while ductility and hardness more accurately reflected the microstructural evolution. Ni and Cu additions to hypereutectic Al–Si alloys promote the formation of stable intermetallics (Al_2Cu, Al_3Ni, Al_3CuNi, Al_7Cu_4Ni) enhancing the high-temperature strength [9]. Notably, the addition of Ni increases the number of θ-Al_2Cu phase pairs and refines their morphology. Several studies have reported that the addition of Ni can significantly improve the high-temperature performance of Al-Si-Cu alloys, increasing the effective operating temperature beyond 200°C. For instance, Liu et al. [10] have demonstrated that the introduction of 1–2 wt% Ni into Al–Si–Cu alloys extended their structural and mechanical stability up to 300°C under sustained thermal and mechanical loading conditions. Similarly, Zhang et al. [11] have observed that the Ni-containing intermetallic phases particularly Al_3Ni and Al_7Cu_4Ni contributed to the enhancement of creep resistance and reduced the degradation at elevated temperatures thereby improving the high-temperature applicability of these alloys. The microstructural refinement due to the addition of Ni and Cu enhances the alloy's resistance to coarsening and degradation. Cu encourages Al_2Cu formation, while Ni promotes the development of Al_3Ni phases both contribute to the strengthening by precipitation and solid-solution mechanisms. These alloying elements also reduce the dendritic arm spacing thereby improving the strength in accordance with the Hall–Petch relationship. Spray forming results in a fine-grained, equiaxed microstructure with a homogeneous distribution of Si, Cu and Ni phases, thereby enhancing the mechanical strength and tribological properties. Mehabubsubahani et al. [2] have found that the spray-deposited Al-15Si-4Ni-2Cu alloy exhibited approximately 24 % higher hardness and significantly reduced the wear rate at temperature up to 300°C as compared to both binary spray-formed and as-cast alloys. Moreover, Lü et al. [12] have examined Al-7Si-1.5Cu-0.4Mg alloy with a low Ni content in it and observed a notable improvement in elevated-temperature mechanical strength above 250°C. Microstructural stabilization by the addition of Ni-Cu reduces coarsening and retention loss at high temperature while maintaining fine dendritic spacing and strong intermetallic network that conform to Hall-Petch strengthening [13]. The combination of Ni-Cu alloying and spray forming thus produces a thermally stable microstructure that preserves the mechanical integrity and wear resistance above 200°C. In the present study, the influence of the addition of nickel (Ni) on the mechanical behavior of spray-formed (SF) Al-15Si-2Cu–xNi alloys was investigated and compared with that of the as-cast (AC) alloys. The aim was to assess the effect of varying Ni content on the microstructure, tensile strength, ductility and hardness of the alloys under both ambient and elevated temperature conditions. Thus the present investigation provides an insight into the role of Ni in enhancing the mechanical performance of hypereutectic Al–15Si–2Cu alloy for high-temperature engineering applications.

2. Materials and methods

In the present study, Al-15Si-2Cu-2Ni, Al-15Si-2Cu-4Ni and Al-15Si-2Cu-6Ni alloys were selected. The elemental composition of the alloys has been listed in Table 1. The as-received ingots of cast alloys (Fenfee Metallurgical, India) were remelted in an electric furnace (SILICARB Recrystallized (P) Ltd., India) and the molten metal was subsequently poured into preheated steel dies to form cylindrical bars.

The synthesis of spray-formed alloys of different composition was performed by varying the process parameters of each alloy as reported in Table 2.

The microstructural features were explored using an optical microscope (Lynax and Zeiss Axio Scan-Z1). The relative phase distribution and grain size were measured by ASTME112–10 by image analysis software (Nascent Technology, Inc.). Scanning Electron Microscopy (SEM) (JEOLJSM-6480LV) was utilized to analyse the microstructure and tensile fractured surface of samples. The phase composition was examined under Energy-Dispersive X-ray (EDX) spectroscopy and SEM was performed at an acceleration voltage of 10–30 kV.

2.1. Hardness testing

The microhardness of the alloys was measured by Vickers hardness Tester (Future Tech Japan: FM3100) complying with the ASTM E384 test method. The hardness test was conducted at a load of 200 g for a dwell period of 15 s. The average of six measurements taken from different locations on each sample was recorded as the representative hardness of the alloys.

2.2. Tensile testing

The tensile specimens were machined from both as-cast (AC) and spray-formed (SF) alloys in accordance with the E8-ASTM standards. Room temperature tensile tests were conducted using standard universal (FIE-UNITEK 9550 & TEC-SOL, India) testing machines. For high-temperature tensile testing, a split-type high-temperature testing machine (MCS-10KN) equipped with a dedicated hot chamber and a suitable stand was used. The equipment conformed to the ASTM E21 and ISO 6892 Part II standards. The furnace was capable of reaching temperatures up to 1200°C and was fitted with three thermocouples with active control on the first and third thermocouples to ensure uniform heating. The temperature variation inside the chamber was maintained within ±3°C. Before testing, samples were held at the target temperature for 15 min to ensure thermal equilibrium throughout the gauge section. A front-facing slot of 25 mm× 60 mm was provided in the furnace for inserting an extensometer for strain measurement. The specimens were aligned along the load axis and securely clamped using two grips. A slight preload was applied to prevent slippage during testing. All tests were performed at a constant nominal strain rate of 0.05 min^{-1} , equivalent to a cross head speed of 0.0083 mm/s. For each alloy composition, five tensile specimens were tested, and the reported results represent the average of five individual measurements.

Table 1
Elemental Composition of the Alloys (wt%).

Alloy Designation	Si	Ni	Cu	Fe	Mg	Al
Al−15Si−2Cu−2Ni A1	15.05	2.01	2.01	0.08	0.006	Bal
Al−15Si−2Cu−4Ni A2	15.04	4.05	2.06	0.04	0.0067	Bal
Al−15Si−2Cu−6Ni A3	15.00	6.01	2.10	0.03	0.0011	Bal

Table 2
Spray forming process parameters.

Alloy Designation	Super heat melt temperature (°C)	Substrate Distance (mm)	Gas pressure (MPa)	Melt flow rate (kg min^{-1})
Al−15Si−2Cu−2Ni S1	940	390	0.45	2.5
Al−15Si−2Cu−4Ni S2	950	400	0.45	2.2
Al−15Si−2Cu−6Ni S3	980	410	0.45	2.5

3. Results and discussion

3.1. XRD analysis

The XRD patterns of the as-cast alloys are shown in Fig. 1(a–c). High-intensity peaks observed in the three AC alloys at 38.6°, 44.8°, 65.2° and 78.3° are attributed to Al (ICDD-00–001–1180). The presence of the Si phase was confirmed from the peaks that appeared at 28.5° and 69° (ICDD-00–001–0787). The peaks are narrower in the A1, A2, and A3 alloys because of their coarser microstructures. This is consistent with the general principle that coarser grains produce sharper diffraction peaks due to reduced macrostrain and lower defect density [14].

The XRD patterns of S1, S2 and S3 alloys are shown in Fig. 1(d–f) respectively. The XRD patterns of the three SF alloys show that the high-intensity peaks at 38.8°, 44.8°, 65.5°, and 78.6° are attributed to Al. The Si phase was confirmed from the peaks that appeared at 28.8° and 69°. The peaks in S1, S2 and S3 alloys are typically broader because of finer microstructures and smaller grain size that arise from the fast-cooling rates in spray forming. The broadening of peaks with reduced grain size is theoretically explained by the Scherrer equation, which relates the peak width to crystallite size and lattice strain [15]. Also, the intensity of SF alloys is higher (0 – 6000c/s) than AC alloys (0 – 3000c/s), which may be attributed to the differences in preferred orientation or phase fraction influenced by the rapid solidification process [16]. In addition to the presence of Al and Si peaks, the common diffraction peaks at angles of 22.09°, 41.84°, 56.5° and 76.5° are attributed to the Al_3Ni phase in the A3 alloy and at 56.5° and 76.5° in the A1, A2, S1, S2, and S3 alloys respectively (ICDD-04–007–0402). The Al_3Ni peak intensity increased as the Ni content increased, confirming the presence of a greater fraction of the Al_3Ni phase. This trend is in agreement with previous studies, which show that addition of Ni promote the formation of Al_3Ni and other Ni-rich intermetallics during solidification in Al-based alloys [17,18]. The appearance of an additional peak at the angle of 47.4° in S1, S2 and S3 alloys and also in A1, A2, and A3 alloys is attributed to the Al_2Cu phase (ICDD-01–080–5762). The formation of Al_2Cu is consistent with Cu-containing aluminum alloys undergoing eutectic reactions during solidification as reported in earlier phase diagram studies [19].

3.2. Microstructural features of as–cast alloys

The Fig. 2(a) displays the optical micrograph of the A1 alloy, which is composed of coarse blocks of primary Si particles, needle/acicular type eutectic Si, blocks of Cu-rich intermetallic phase. The microstructure revealed a network of short strip-like features along with a reticulated Ni-rich intermetallic phase distributed within the interdendritic regions of the matrix. Additionally, the primary silicon particles, with an average size of 155 ± 5 μm, were observed as sharp-edged, blocky structures. The Fig. 2(b)&(c) display the microstructures of the A2 and A3 alloys respectively. They consist of primary α-Al dendrites, primary Si blocks, and eutectic Si surrounding their boundaries.

The addition of Ni has no effect on the morphology or size of the primary Si phase or eutectic Si phase which are gray in color. The θ-Al_2Cu phase (white contrast) exists in the form of Chinese script. The fraction of Al_3Ni phase clearly increased at high Ni concentration and the morphology of the Al_2Cu phase changed from strip-shape to fishbone-shape. On the other hand, eutectic Si and Al_3Ni phase are difficult to discern from one another on the basis of optical image contrast. The average size of Al_3Ni phase for A1, A2 and A3 alloys are 16.52, 18.94, and 21.21 μm respectively. Additionally, the average Si phase size increases with increasing Ni content. The average particle size of primary Si was 10.32, 14.04 and 16.62 μm for A1, A2 and A3 alloys respectively. Using Image-Pro Plus analyzer, mean diameter and phase volume percentage were measured as reported in Table 3. The average grain sizes of A1, A2, and A3 alloys are 12, 6.7, and 5.6 μm respectively. This shows that the alloy's grain size decreases as the Ni concentration increases. This grain refinement behavior aligns with previous findings that intermetallic particles such as Al_3Ni act as heterogeneous nucleation sites and pin grain boundaries, thereby restricting grain growth during solidification [20]. This grain refinement is due to the formation of intermetallic compounds between Ni and other elements (such as Al and Si), which impedes the growth of grains during the solidification process. As a result, the addition of Ni refines the silicon particles. This effect is also supported by thermodynamic modeling and microstructural observation in Al-Si based systems containing Ni, where the formation of Ni-containing intermetallics retards dendritic growth and promotes nucleation of refined eutectic structures [21]. The occurrence of nickel silicides (such as NiSi, Ni_2Si etc.) is responsible for this phenomenon. These nickel silicides act as nucleation sites for primary Si, thereby reducing its size and distributing it more uniformly. As reported by Jiang et al. [22] nickel silicides lower the nucleation barrier for Si crystallization, enhancing the formation of fine homogeneously distributed Si particles. The Ni content in hypereutectic Al–Si–Cu alloys tends to form complex intermetallic compounds such as Al_3Ni, Al_3Cu_4Ni and others with Al-Si-Cu alloys. The increased Ni content enhances the overall microstructural refinement. This includes the primary α—Al phase, eutectic Si and other phases present in the microstructure. These observations align with the solidification behavior described by Reddy et al. [23]. They have reported that Ni-rich phases promote grain refinement and enhance high-temperature performance through structural stabilization.

The quantitative phase analysis of the A1, A2 and A3 alloys by image analyzer is shown in Table 4. The area percentage of Si clearly decreases marginally with increasing Ni content and the number of eutectic Si phases decreases. An increase in the Ni content from 2 to 6 wt% resulted in an increase in the Al_3Ni intermetallic phase area from 26.3 % to 34.2 % (Table 4).

The Fig. 3(a) shows the SEM/EDS micrograph of the A1 alloy. The A1 alloy exhibits a typical hypereutectic morphology consisting of coarse primary Si particles embedded in the Al matrix. These primary Si particles appear in angular and faceted form and a network of eutectic silicon is observed in fine, fibrous or acicular form non-uniformly distributed throughout the matrix.

Additionally, bright script-like and needle-shaped intermetallic phases are evident, likely consisting of Ni and Cu-based compounds such as Al_3Ni, Al_2Cu and Al_3CuNi. These intermetallics are predominantly located in the inter dendritic regions, formed during the final stage of solidification. The Fig. 3(b) presents the EDS spectra of the A1 alloy obtained from different spots within the microstructure. Table 5 presents the EDS results of the chemical composition of the different phases. The spectra spots 1, 2, 3, 4, 5 and 6 are identified as primary Si, Al_3Ni, θ-Al_2Cu intermetallic, eutectic Si, Al_3CuNi and α-Al phases respectively (Fig. 3(a)). The δ-Al_3Ni phase and ε-Al_3CuNi white phase appeared as interconnected reticular networks, strip-like formations and fishbone structures.

The Fig. 4(a) shows the SEM/EDS microstructure of the A2 alloy. Compared to the A1 alloy, the A2 alloy revealed a significant increase in the volume fraction of intermetallic phases. Both alloys contain coarse, angular primary silicon particles; however, the A2 alloy shows a denser distribution of Ni-rich intermetallics, which appear in script-like and blocky form, concentrated primarily in the inter dendritic regions. The increased Ni content in the A2 alloy promotes the formation of complex Al-Ni-Cu-Si intermetallic compounds, resulting in a more fragmented and discontinuous Al matrix. Notably, the A2 alloy exhibits the appearance of rod-like secondary phases along with the fiber-like Al_3Ni in greater volume. The θ-Al_2Cu phase is observed in a rod-like form, while the ε-(Al_3CuNi) phase appears as multiple separate short rods. Additionally, the volume fraction of both δ and ε phases are higher in the A2 alloy than in the A1 alloy.

The EDS analysis of the A2 alloy as shown in the Fig. 4(b) provides the elemental composition of ε intermetallic at spot-1. The spectrum spots 5 and 6 confirm the formation of significant Ni-rich intermetallic

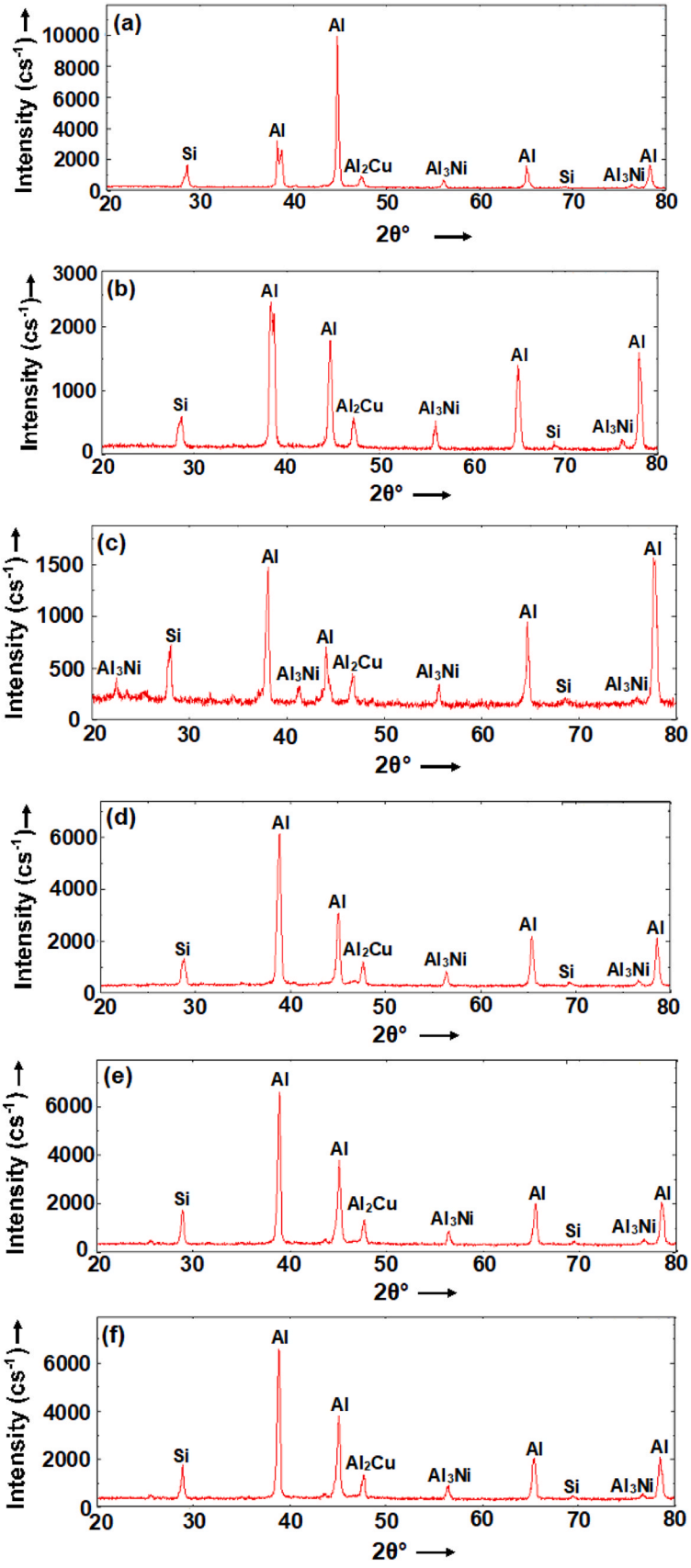

Fig. 1. XRD patterns of **(a)** A1; **(b)** A2; **(c)** A3; **(d)** S1; **(e)** S2 and **(f)** S3 alloys.

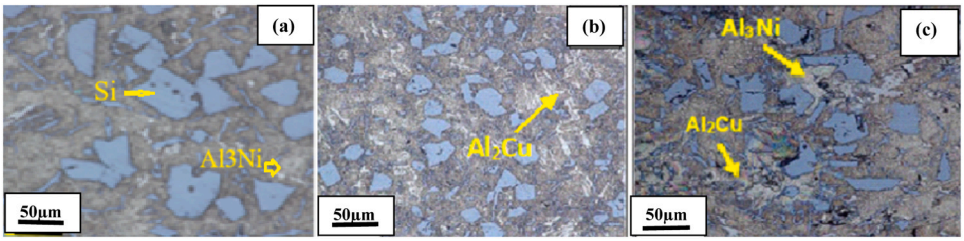

Fig. 2. Optical micrographs of AC alloys **(a)** A1 alloy; **(b)** A2 alloy; **(c)** A3 alloy.

Table 3
Average grain size, grain area and volume fraction of phase alloys.

Alloy	Average Diameter (µm)	Average Grain Area (µm)	Grain No.
A1	12	126	10
A2	6.7	44.6	11
A3	5.6	31.5	12

Table 4
Phase composition of AC alloys.

Phase	**Area %**		
	A1	**A2**	**A3**
Primary Si	9.20	9.03	8.7
Eutectic Si	42.74	39.48	36.66
Al_3Ni	26.3	30.43	34.22
Al_2Cu	10.32	9.83	7.04

phases such as Al_3Ni and ε-(Al_3CuNi). A small amount of iron (0.43 wt%) may be attributed to Fe-based intermetallics or impurities while the oxygen content (2.22 wt%) likely results from the surface oxidation during sample preparation. Table 6 outlines the EDS results obtained for the individual phases present in the A2 alloy.

The Fig. 5(a) presents the SEM/EDS microstructure of the as-cast A3 alloy, which clearly exhibits the presence of primary Si particles, eutectic Si, α-Al grains, and various intermetallic phases. The primary Si particles appear to be randomly distributed with a block-like morphology, particularly noticeable at spot 2 in the micrograph. These particles range in size approximately from 50 to 150 µm. Eutectic Si particles, in contrast, exhibit a rod-like or acicular morphology with a high aspect ratio, forming in the inter dendritic regions. The presence of these Si phases was further confirmed by the EDS spectrum shown in Fig. 5(b) and supported by XRD analysis. In addition to the silicon phases, the microstructure includes distinct intermetallic compounds. Chinese-script-like Al_2Cu is identified, as indicated by the EDS data at spot 6 in Fig. 6(a). Notably, Ni-rich intermetallic phases such as Al_3Ni and Al_3CuNi are also observed at spots 1 and 3. These appear as coarse, non-interconnected fishbone or fibre-like structures. The volume fraction and size of these Ni-rich intermetallics are significantly higher in A3 alloy compared to the A2 alloy. The increase in Ni content promotes the formation and growth of the Al_3Ni phase, which becomes more prominent as the alloy reaches saturation levels of Ni during solidification. The higher Ni concentration not only increases the quantity of Al_3Ni but also provides more nucleation sites for its formation. As a result, the Al_3Ni phase becomes larger and more numerous.

The availability of Ni in the molten alloy directly influences the size and morphology of these intermetallics. With continued increase in Ni content, the Al_3Ni particles may evolve in complexity and size. Additionally, the elevated Ni level enhances the formation of Al_3CuNi by allowing more Ni atoms to combine with Cu and Al. This is due to the increased chemical activity and mutual solubility of Ni with Al and Cu at elevated temperatures, which facilitates the nucleation of ternary intermetallic compounds. Before the formation of Al_3CuNi, other phases such as Al_3Ni and Al_2Cu may form, and these can coexist or even transform under certain solidification conditions. According to phase equilibrium studies and solidification simulation, Al_3Ni typically forms at higher temperatures and acts as a precursor phase, while Al_2Cu appears during eutectic reaction. As cooling continues, and with the presence of sufficient Ni and Cu, the Al_3CuNi phase can form either directly or through a peritectic or eutectoid transformation from these precursor phases [24]. The evolution of these phases depends on the local composition, cooling rate, and nucleation kinetics.

Experimental results from piston-grade Al-Si-Cu-Ni alloys also confirm that with increasing Ni content, the fraction of Al_3CuNi increases, contributing to the improved thermal stability and strength at elevated temperatures [25]. Compared to the A1 alloy, which has a relatively balanced microstructure with moderate intermetallic presence, the A2 alloy, exhibits localized but increased Ni-rich phase formation and the A3 alloy displays a heavily reinforced structure. The dense and coarse distribution of intermetallics in A3 alloy significantly alters the continuity of the Al matrix, which may improve the mechanical strength and thermal resistance but can potentially reduce ductility. Table 7 provides the detailed phase composition of the A3 alloy supporting the microstructural observation and confirming the increased formation of Ni-rich intermetallics with higher Ni content.

3.3. *Microstructural features of spray formed (SF) alloys*

The optical microstructures of SF alloys are shown in the Fig. 6. The S1 alloy (Fig. 6(a)) consisted of spherical shaped Si phases exhibited a homogeneous distribution within the equiaxed Al matrix. The optical micrographs of S2 and S3 alloys as shown in Fig. 6(b) and (c), reveal fine, spherical primary Si and eutectic Si phases, along with finely dispersed Ni-rich and Cu-rich intermetallic particles (appearing as white contrast), uniformly distributed within the equiaxed Al matrix. The Cu and Ni intermetallic particles range in size from 10 to 20 µm and have an aspect ratio of 7 ± 1.3, whereas the primary Si particles are 40 ± 1.7 µm in size and have an aspect ratio of 1.5 ± 0.26. The intermetallic phase size clearly increases with increasing Ni content, which is uniformly distributed in the matrix and has a spherical, round-edged rod shape. The average grain size and average grain area of the alloys were measured by the intercept method. The average grain size of S1 alloy is greater than that of S2, and S3 alloys (Table 8). Additionally, the grain size decreases with increasing Ni content.

The Fig. 7 presents the SEM and EDS micrographs of S1, S2 and S3 alloys. It is evident that the SF alloys exhibit notable variations in phase formation and distribution with increasing nickel content. In the S1 alloy, the microstructure mainly consists of finely distributed primary Si particles in the Al matrix. The Ni-rich intermetallic phases, such as Al_3Ni and Al_9FeNi are present in small quantities and appear as fine, dispersed particles with an average size ranging from 5 to 15 µm. These phases are uniformly distributed and do not form networks or clusters (Fig. 7(a)). In the S2 alloy, with an increased Ni content of 4 wt%, there is a noticeable increase in the volume fraction of the Ni-rich intermetallics. The phases identified include Al_3Ni and Al_3CuNi which are more abundant and are observed predominantly along the grain boundaries. The intermetallic phases slightly exhibit coarser morphology with average sizes between 10 and 30 µm. The distribution is relatively uniform although localized

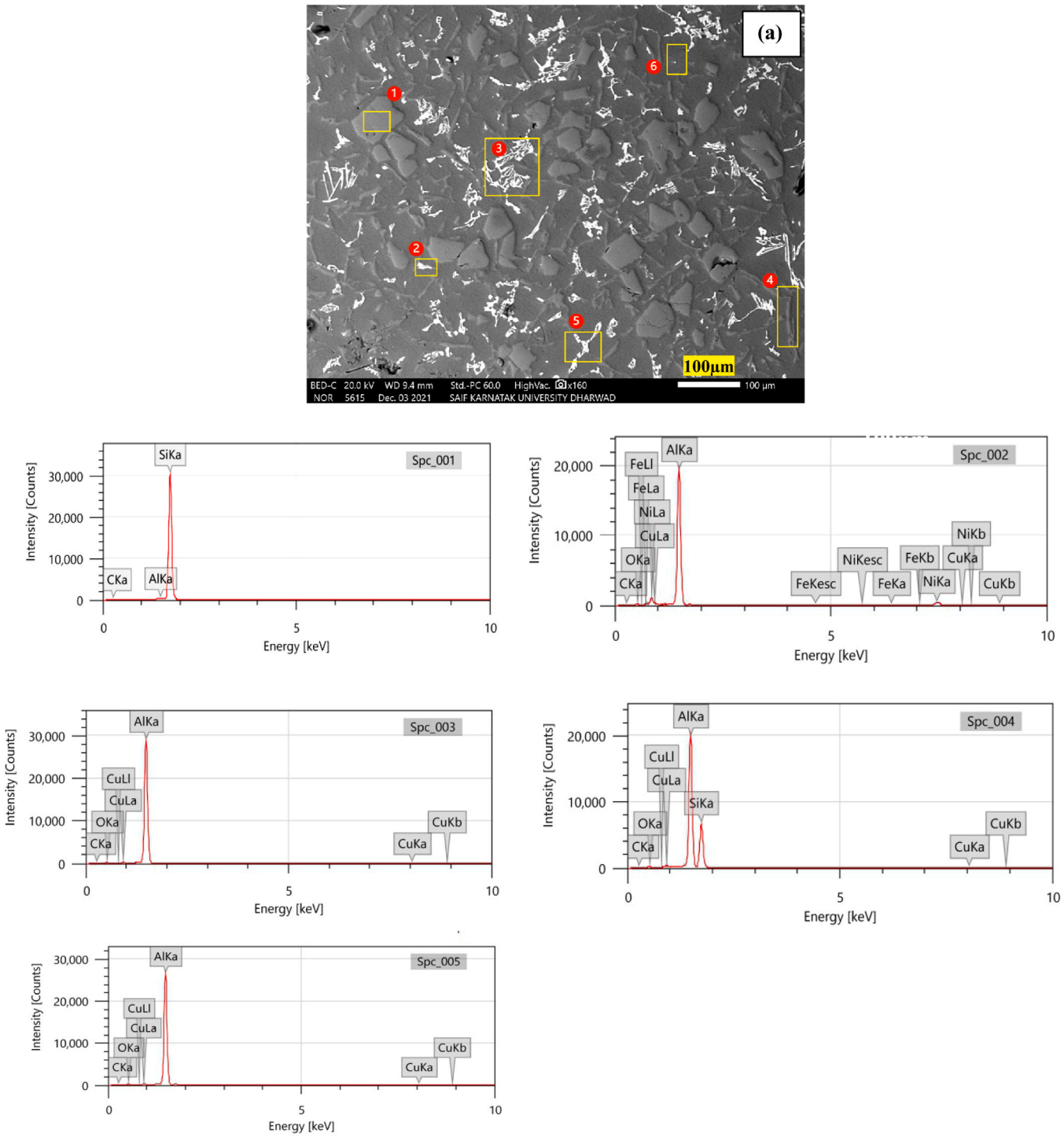

Fig. 3. **(a)** SEM/EDS micrograph & **(b)** EDS spectra of A1 alloy.

clustering is observed, indicating the early stages of phase coarsening (Fig. 7(b)). The S3 alloy, containing 6 wt% Ni, displays a substantial increase in the amount and size of the Ni-rich intermetallics. The phases Al_3Ni, Al_3CuNi and Al_9FeNi are present in higher volume fractions and form interconnected networks and blocky morphology. The average phase size ranges from 20 to 40 µm (Fig. 7(c)). The increased Ni content leads to phase coarsening and the formation of complex, multi-phase regions. Comparatively, the S1 alloy exhibits the finest and most homogeneous phase distribution, while the S2 alloy shows a balanced microstructure with an optimal combination of phase refinement and volume fraction. The S3 alloy, although rich in strengthening phases, demonstrates excessive coarsening and network formation. The EDS results depicting the phase composition of S1, S2 and S3 alloys at different spectral locations are shown in Table 9, Table 10 and Table 11 respectively.

The spray formed Al-Si-Cu-Ni alloy exhibits a refined and uniform

Table 5
EDS results of the A1 alloy at different spectral locations.

Wt. (%)				
Spectral point	Al	Si	Ni	Cu
1	0.38	98.54	-	-
2	74.91	—	23.35	1.45
3	84.82	—	–	11.17
4	54.12	34.13	0.12	1.18
5	85.61	0.00	08.59	6.40
6	98.12	1.25	——	0.63

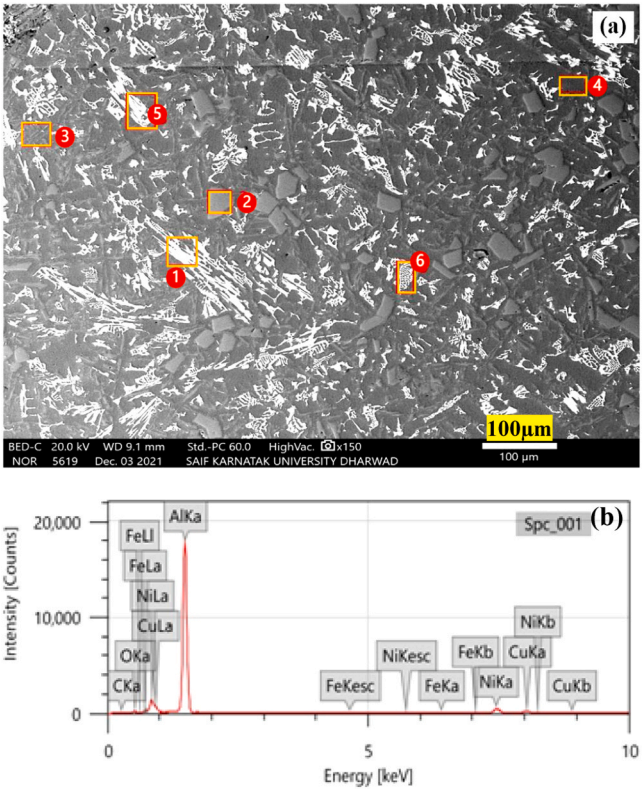

Fig. 4. (a) SEM/EDS micrograph & **(b)** EDS spectrum of the A2 alloy (spot-1).

Table 6
Phase composition of the A2 alloy at different spectral locations.

			Wt (%)		
Spectral location	**Phase**	**Al**	**Si**	**Ni**	**Cu**
1	δ-Al_3CuNi	69.62	0.73	13.30	7.41
2	Primary-Si	1.85	97.54	0.33	0.28
3	Eutectic-Si	44.18	53.42	0.41	1.99
4	α-Matrix	96.97	1.16	0.41	1.41
5	ε-Al_3Ni	70.9	—	27.45	1.02
6	θ-Al_2Cu	66.13	0.01	1.02	32.86

distribution of Si and intermetallic phases due to the increased cooling rate during atomization. Significant undercooling of the droplets prior to the nucleation of primary Si promotes refinement, while the reduced deposition temperature suppresses phase growth. Consequently, fine Si particles, Ni-rich intermetallics, and a higher number of Al_2Cu precipitates are observed in the spray formed structure. The dendritic and Chinese-script morphology typical of as-cast alloys are significantly modified, making it difficult to distinguish between the primary θ, δ, and ε phases. The evolution of microstructure in spray formed hypereutectic Al-Si alloys has been attributed to rapid cooling, droplet fragmentation, and impact during deposition, resulting in equiaxed grains and fine Si

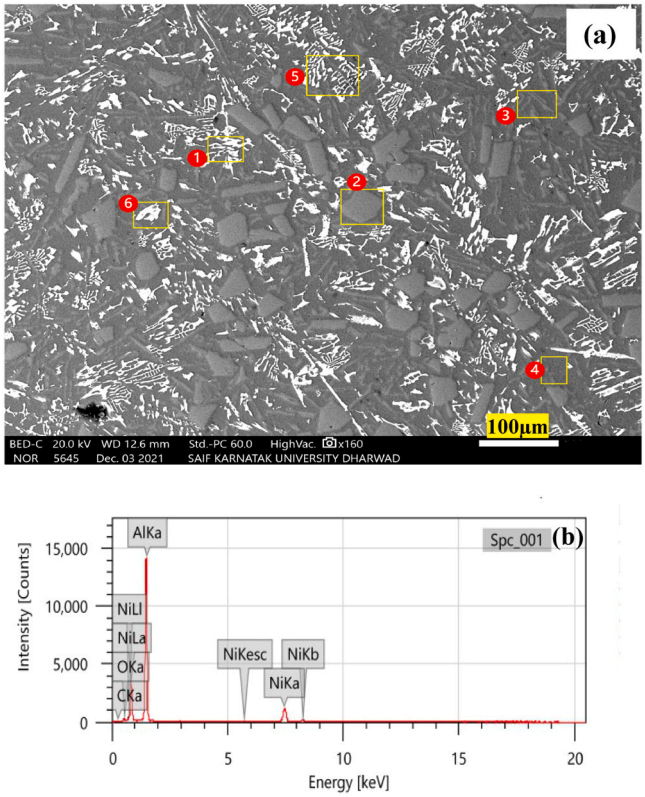

Fig. 5. (a). SEM/EDS micrograph &**(b)** EDS spectrum (spot-1) of the as-cast A3 alloy.

dispersion. In Al-Si-Cu-Ni systems, the solidification sequence deviates from the equilibrium pathways. It is assumed that solidification begins with the formation of intermetallic δ-Al_3Ni and ε-Al_3CuNi phases, followed by primary Si nucleation on δ-Al_3Ni, with the remaining liquid solidifying into an irregular eutectic of α-Al, Si and Al_2Cu. According to Zhou et al. [26], the spray deposited microstructure contains both eutectic and primary Si, with a predominance of metastable δ and ε phases. The volume fraction of ε-Al_3CuNi is higher than that of the equilibrium δ phase. This can be attributed to the alloy's strong tendency to form metastable phases during atomization and the sluggish transformation kinetics to equilibrium phases. The δ-Al_3Ni phase formation is influenced by the thermal conditions during solidification. Spray deposition occurs in two stages: rapid solidification during gas atomization and slower cooling during droplet consolidation. The ε-phase may form within droplets before deposition and can transform into δ-Al_3Ni due to the slower cooling rate after deposition, acting as a short term annealing effect [27].

3.4. Mechanical properties

3.4.1. Hardness of AC and SF alloys

The variation in hardness of the AC and SF alloys at different temperatures is presented in Fig. 8. The data clearly shows that the SF alloys consistently exhibit higher hardness than their AC counterparts across the entire evaluated temperature range (30°C to 300°C). At 30°C, the hardness of the SF alloy is 142 HV compared to 112 HV for the AC alloy, reflecting an increase of approximately 26.8 % (Fig. 8(a)). This enhancement is attributed to the rapid solidification during the spray forming process, which refines and homogenizes the distribution of primary Si and intermetallic phases. At 100°C, the hardness of the SF alloy decreases slightly to 136 HV, while the AC alloy registers 105 HV, maintaining a 29.5 % improvement in the SF alloy (Fig. 8(b)). The higher retention of hardness at elevated temperatures suggests greater

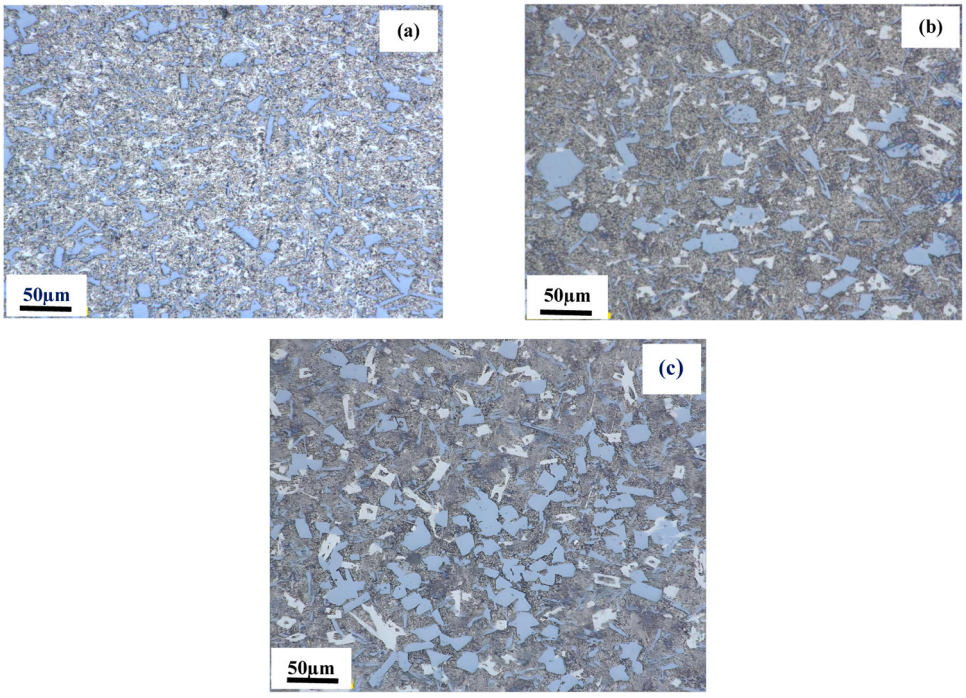

Fig. 6. Optical micrographs of spray formed **(a)** S1 **(b)** S2 and **(c)** S3 alloys.

Table 7
Phase composition of the A3 alloy at different spectral locations.

Spectral point/Phase	Al	Si	Ni	Cu
1. δ-Al_3CuNi	64.16	0.73	15.36	21.16
2. Primary Si	2.55	96.54	0.13	0.18
3. Eutectic Si	48.18	49.22	0.20	1.09
4. α-Matrix	96.27	2.26	0.31	1.02
5. θ-Al_2Cu	70.25	1.04	0.39	26.37
6. Al_3Ni	67.2	—	32.75	0.03

Table 8
Average grain size and area of the SF alloys.

Alloy	Average Diameter (mm)	Average Grain Area (mm^2)
S1	0.009	0.00036
S2	0.006	0.00026
S3	0.004	0.00016

thermal stability of Ni- and Cu-rich intermetallics such as Al_3Ni, Al_2Cu and Al_3CuNi which remain more stable and resist coarsening under thermal exposure [28]. At 200°C, the hardness further decreases to 127 HV for the SF alloy and 98 HV for the AC alloy. Despite this drop, the SF alloy retains a 29.6 % higher hardness (Fig. 8(c)).

The finer microstructure in the SF alloy slows the softening process by retarding the diffusion-driven coarsening of strengthening phases, such as θ-Al_2Cu and δ-Al_3CuNi [29]. At 300°C, the spray formed (SF) alloy exhibits a hardness of 115 HV, whereas the as-cast (AC) counterpart demonstrates a reduced value of 89 HV (Fig. 8(d)). This corresponds to a 29.2 % enhancement in high temperature hardness for the SF alloy. This trend confirms that the SF microstructure offers superior thermal resistance, with enhanced phase stability and grain boundary pinning effects due to the refined intermetallics. A uniformly equiaxed Al matrix contains finely distributed primary and eutectic silicon, along with thermally stable intermetallic phases (θ, ε and δ), accompanied by increased solid solubility of alloying elements contributes to the enhanced hardness and temperature resilience of the SF alloys. These microstructural features, supported by rapid solidification theory, provide multiple barriers to dislocation movement, thereby improving the alloy's overall mechanical response [30].

The presence of intermetallic phases in the SF alloys significantly reduces the matrix ductility, resulting in enhanced hardness. These particles impede the motion of dislocations during deformation, thereby increasing the resistance to plastic flow and improving the hardness of the alloy. The relationship between grain size and hardness is described by the Hall–Petch equation [31]

$$H_v = Hv_o + \cdot kH_v d^{-1/3} \quad (1)$$

Where H_v denotes the hardness of the polycrystalline metal
'd' represents the grain size
$Hv_o \cdot \& \cdot kH_v$ are constants

According to Eq. (1), a reduction in grain size leads to an increase in hardness. The higher hardness observed in the SF alloys at ambient temperature is primarily attributed to the refined grain size of the Si phase and the presence of thermally stable intermetallics such as Al_2Cu, Al_3Ni, and Al_3CuNi. These phases act as obstacles to the dislocation movement, thereby enhancing the localized resistance to plastic deformation. The effect of temperature on hardness is expressed by the Eq. (2) [32]

$$H_v \cdot = \cdot Ae^{-BT} \quad (2)$$

where ^{A} and ^{B} are constants
^{T} is the test temperature (°K)

The Eq. (2) indicates that the hardness decreases exponentially with increasing temperature. This behavior is observed in both AC and SF alloys, where the reduction in hardness at elevated temperatures is attributed to the increased atomic vibration, which reduce the material's resistance to indentation. Among the studied compositions, the S1 alloy exhibited lower hardness at elevated temperatures compared to the S2 and S3 alloys. The reduced thermal stability of the eutectic Si and Al matrix phases in S1 alloy contributed to this decrease. In contrast, the S2 and S3 alloys demonstrated better retention of hardness at high temperatures, which is attributed to the presence of intermetallic phases such as Al_3Ni, Al_2Cu, and Al_3CuNi, likely in their thermodynamically stable forms. Additionally, the reduced softening of the eutectic Si and

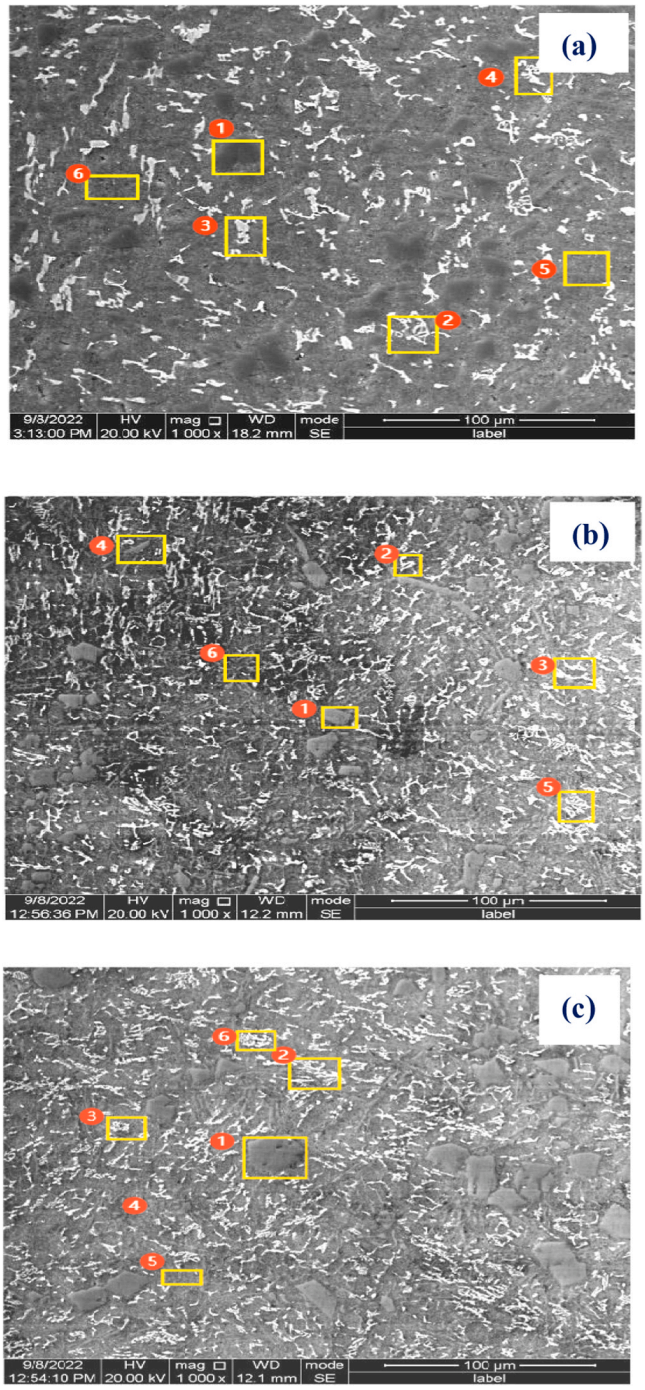

Fig. 7. (a) SEM/EDS micrographs of spray formed (a) S1 (b) S2 and (c) S3 alloys.

Table 9
EDS results of the phase composition of S1 alloy at different spectral locations.

Spectral point	Phase	Al	Si	Ni	Cu
Point 1	Primary-Si	2.18	97.01	0.30	0.51
Point 2	θ-Al_2Cu	65.37	1.26	0.13	33.24
Point 3	δ-Al_3Ni	74.76	—	24.47	0.77
Point 4	ε-Al_3CuNi	68.13	—	17.08	10.79
Point 5	α-Al matrix	81.37	12.7	0.13	5.80
Point 6	Eutectic Si	58.56	38.81	1.25	1.57

Table 10
EDS results showing the phase composition of S2 at different spectral locations.

Spectral point	Phase	Al	Si	Ni	Cu
Point 1	Primary Si	1.28	98.29	0.18	0.24
Point 2	Al_3CuNi	60.13	0.14	22.91	16.79
Point 3	Al_3Ni	74.23	—	25.70	—
Point 4	Eutectic Si	78.41	17.05	0.16	4.38
Point 5	A_2Cu	57.15	2.14	—	41.14
Point 6	α-Al matrix	80.37	12.7	0.15	6.20

Table 11
EDS results of the phase composition of S3 alloy at different spectral locations.

Spectral point	Phase	Al	Si	Ni	Cu
Point 1	Primary Si	4.26	95.21	0.26	0.27
Point 2	Al_3Ni	72.08	0.22	30.69	——
Point 3	Al_3CuNi	68.37	0.52	17.67	13.47
Point 4	α-Al matrix	81.37	11.7	0.13	6.18
Point 5	Eutectic Si	84.33	14.17	0.45	1.02
Point 6	θ-Al_2Cu	65.37	0.26	0.13	34.24

Al matrix in these alloys enhanced their resistance to plastic deformation under thermal exposure.

3.4.2. *Tensile properties of AC and SF alloys*

The Fig. 9 depicts the ultimate tensile strength (UTS) of AC and SF alloys. The Fig. 9(a) shows a consistent decrease in the ultimate tensile strength (UTS) of A1, A2 and A3 alloys as the testing temperature increases from room temperature (RT) of 30°C to 300°C. For all the three alloys, the highest UTS is observed at RT, while the lowest occurs at 300°C. Among the alloys, A3 alloy consistently exhibits the highest UTS across all temperatures, followed by A2 and then A1 alloys. The Fig. 9(b) presents the UTS of SF alloys (S1, S2, S3), which remained higher than those of AC alloys at all temperatures. While the UTS of SF alloys also decreased with temperature, the reduction was comparatively moderate around 10–17 % at 100°C and only 4–6 % at 250°C. Among the SF alloys, S3 alloy maintained the highest UTS throughout the temperature range. On comparison between Figs. 9(a) and 9(b), it is evident that SF alloys outperform AC alloys in terms of tensile strength at both ambient and elevated temperatures. The superior thermal stability of SF alloys is attributed to their refined microstructure, particularly the presence of fine intermetallic compounds and silicon particles, which hinder dislocation movement and delay softening at high temperatures.

The data presented in Table 12 illustrate the decrease in the ultimate tensile strength (UTS) of AC alloys as the temperature increases. The reduction in UTS for alloys A1, A2 and A3 shows a lower range, varying between 5.3 % and 14.55 % with increasing temperature. These results indicate that the decrease in UTS with increasing temperature is less pronounced in the Cu- and Ni-alloyed alloys than in the binary alloy. Table 13 shows the increase in UTS of the SF alloys at different temperatures compared with that of the AC alloys. Compared to their AC counterparts, the UTS of S1, S2 and S3 alloys is high at both room and elevated temperatures. The UTS of all the SF alloys are 25 % and 30 % and 25–47 % higher compared to AC alloys at RT and 300°C respectively. This behaviour can be supported by the presence of thermally stable intermetallic phases such as Al_3Ni, Al_2Cu, and Al_3CuNi which have high melting points and strengthen the matrix by impeding dislocation motion at elevated temperatures [21]. Moreover, the refined and uniformly distributed Si particles and intermetallics resulting from the rapid solidification of spray forming contribute to higher strength retention. Studies have shown that Ni additions promote the formation of fine, heat-resistant intermetallic compounds which inhibit grain boundary sliding and retard phase coarsening under thermal stress [33].

Table 14 shows the reduction in the UTS of the SF alloys with increasing temperature. The results indicate that the percentage decrease in the UTS with increasing temperature is minimal.

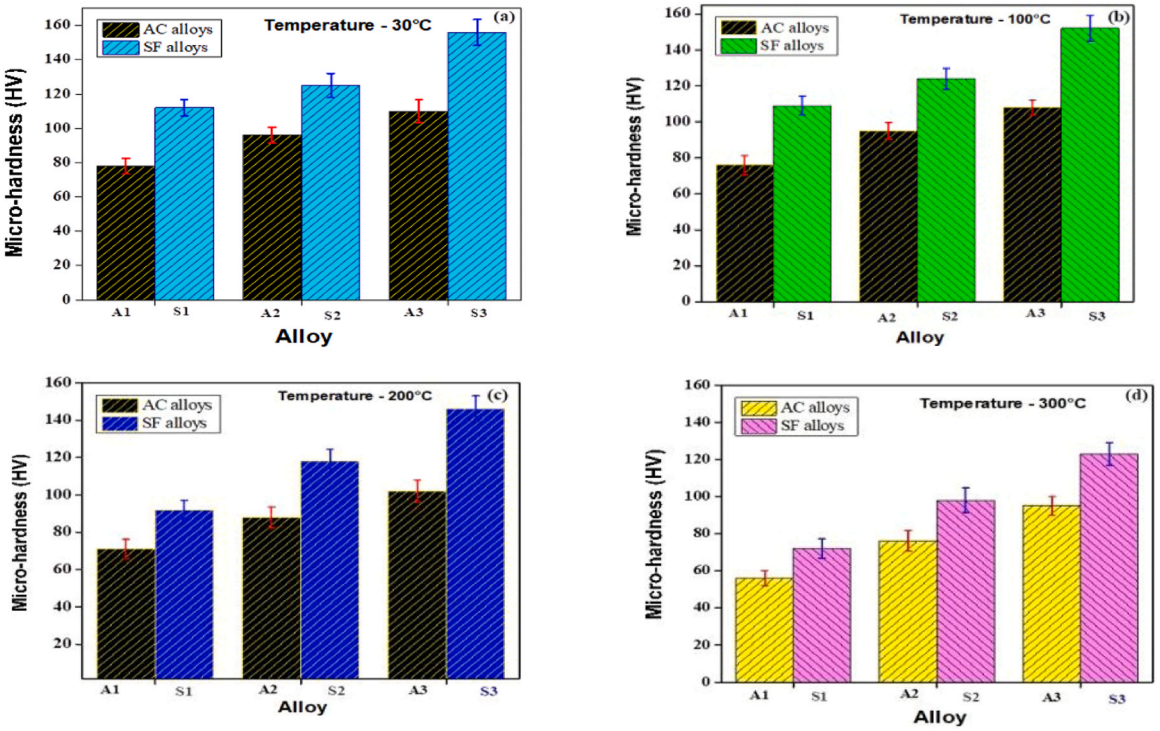

Fig. 8. Hardness of AC and SF alloys at **(a)** 30°C, (b) 100°C, **(c)** 200°C and **(d)** 300°C.

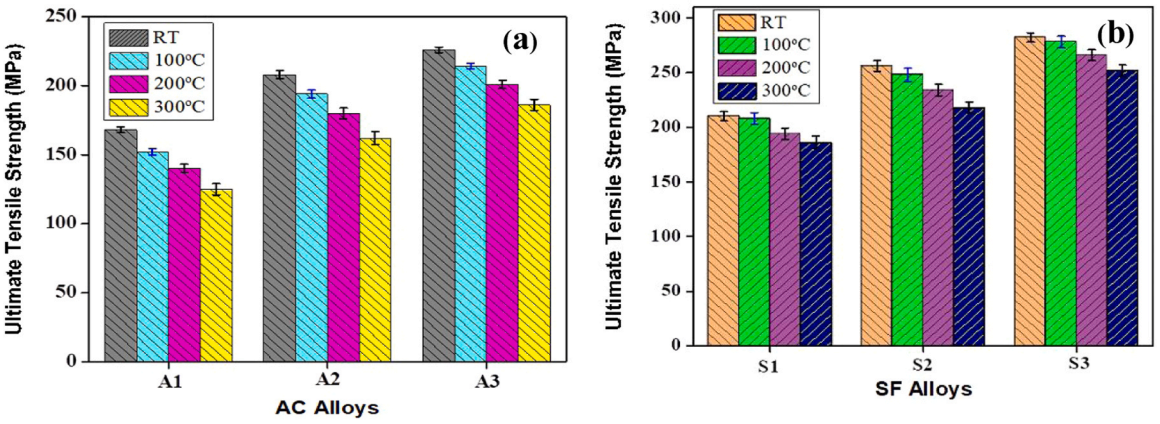

Fig. 9. UTS of (a) AC and (b) SF alloys at different temperatures.

Table 12
Decrease in UTS (%) with increasing temperature.

Alloy	A1	A2	A3
Temperature (°C)	% Reduction	% Reduction	% Reduction
100°C	9.72 %	9.52 %	11.42 %
200°C	16.9 %	11.92 %	11.5 %
300°C	24.55 %	22.85 %	17.46 %

Table 13
Increase in the UTS of SF alloys compared with that of AC alloys.

Temperature/Alloy	S1	S2	S3
30°C	33.30 %	25.0 %	24.70 %
100°C	29.50 %	29.72 %	19.50 %
200°C	23.68 %	32.07 %	32.30 %
300°C	27.70 %	38.50 %	42.00 %

Table 14
Reduction in the UTS of SF alloys with temperature.

Alloy	S1	S2	S3
Temperature (°C)	% Reduction	% Reduction	% Reduction
100°C	5.273 %	3.13 %	1.42 %
200°C	6.46 %	5.6 %	4.32 %
300°C	8.82 %	6.83 %	5.20 %

The Fig. 10(a) illustrates the variation in yield strength (YS) of the AC alloys with temperature. A consistent decline in YS is observed with increasing temperature across all compositions. At 30°C, A2 alloy shows a 17 % increase in YS compared to A1 alloy, while A3 alloy exhibits an additional 11.23 % increase over A2 alloy, resulting in a cumulative improvement of approximately 30 % from A1 alloy to A3 alloy. As the temperature rises, the YS of all alloys decreases, but the rate of reduction is notably lower in the Ni-enriched compositions. Specifically, at 100°C, the YS reduction is 7.9 % for A1 alloy, 7.48 % for A2 alloy, and 5.5 % for

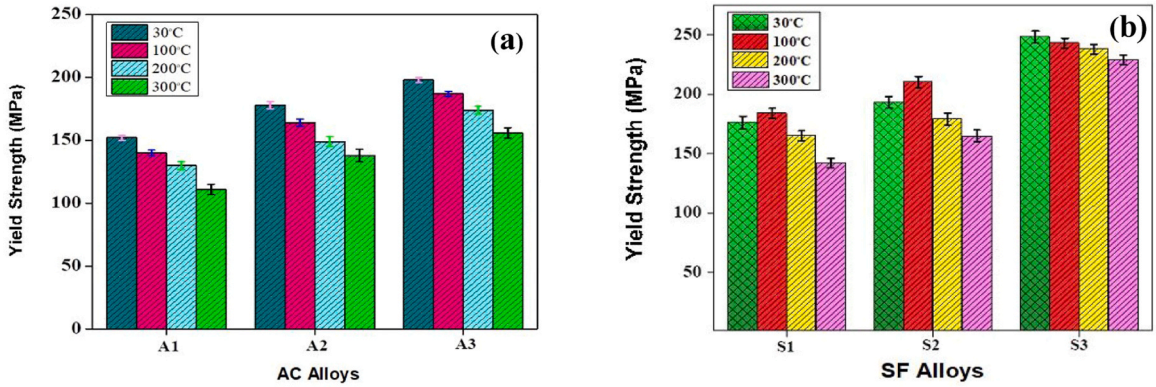

Fig. 10. Yield strength of **(a)** AC and **(b)** SF alloys at different temperatures.

A3 alloy. At 200°C, the respective reductions are 8.45 %, 7.19 %, and 6.9 %. At 300°C, A1 alloy shows a 15.38 % reduction in YS, while A2 and A3 alloys experience lower reductions of 13.58 % and 10.4 %, respectively. These values clearly demonstrate that the increase in Ni content enhances the thermal stability of the AC alloys, with A3 alloy consistently exhibiting the least degradation in strength across all temperatures. The data in Table 15 confirms this trend, underscoring the role of Ni in stabilizing the mechanical properties at elevated temperatures.

The Fig. 10(b) depicts the YS behavior of the SF alloys with respect to temperature, revealing superior performance compared to their as-cast counterparts across the entire temperature range. At room temperature, the YS of S1, S2 and S3 alloys is higher than that of their respective AC alloys by 15.8 %, 17.4 %, and 25.4 %. This improvement becomes more pronounced at elevated temperatures. At 100°C, the YS values of S1, S2 and S3 alloys are higher by 31.4 %, 22 %, and 30 % respectively. At 200°C, the YS values are 27 %, 21 %, and 36 % while at 300°C, the YS of S1, S2 and S3 alloys surpass their AC counterparts by 33 %, 21 % and 46.7 % respectively. These results demonstrate that the SF process significantly enhances the yield strength, particularly under thermal exposure, with the highest gain observed in S3 alloy due to its higher Ni content and refined microstructure. Furthermore, Table 16 shows that the percentage reduction in YS with temperature is less pronounced in the SF alloys compared to the AC alloys. From room temperature to 100°C, the reduction in YS is limited to 5 % for S1 alloy, 4.64 % for S2 alloy and only 2 % for S3 alloy. At 200°C, the respective reductions are 6.47 %, 5.43 %, and 2.05 %, while at 300°C, they reach 10.6 %, 6.89 %, and 3.7 %. These findings highlight the enhanced thermal stability of the SF alloys, particularly S3 alloy, which consistently exhibits minimal strength degradation with temperature. The combined influence of Ni addition and the uniform, fine-grained microstructure resulting from spray forming contributes to the superior mechanical performance and thermal resistance of the SF alloys. Thus, both compositional modification and processing technique **(b)**

play critical roles in optimizing the yield strength and its retention at elevated temperatures.

The Fig. 11 illustrates the variation in percent elongation (%δ) of the AC and SF alloys at different temperatures. In Fig. 11(a), the AC alloys show a general trend of increasing elongation with temperature. For A1 alloy, the elongation increases from 7.3 % at room temperature to 11.57 % at 300°C. A similar trend is observed for A2 and A3 alloys, where the elongation rises from 5.67 % to 9.17 % and from 4.56 % to 8.89 % respectively, over the same temperature range. Notably, there is a slight reduction in elongation for all AC alloys when the temperature increases from 30°C to 100°C, followed by a significant increase between 200°C and 300°C, indicating that higher temperatures promote ductility by facilitating dislocation mobility and reducing flow stress. Among the AC alloys, A1 alloy consistently exhibits the highest ductility at all temperatures, whereas A3 alloy, which contains a higher Ni content, shows the lowest elongation, likely due to the increased volume fraction of intermetallics that hinder plastic deformation. In contrast, Fig. 11(b) shows that the SF alloys exhibit substantially higher elongation values than their AC counterparts across all temperatures, indicating superior ductility as a result of the refined and homogeneous microstructure produced by the spray forming process. For S1 alloy, the elongation increases from 12.2 % at 30°C to 19 % at 300°C. Similarly, S2 alloy shows an increase from 11.5 % to 15 %, and S3 alloy from 10.5–14 % over the same temperature range. Unlike the AC alloys, the SF alloys show a progressive increase in elongation with temperature, with no initial drop, indicating improved thermal stability and deformation characteristics. However, the total elongation decreases with increasing Ni content across the SF alloys, with S3 alloy consistently exhibiting lower ductility than S1 and S2 alloys. This reduction in ductility with higher Ni levels is attributable to the presence of a greater amount of Ni-rich intermetallics that act as stress concentrators and restrict matrix plasticity. The enhanced elongation in SF alloys can be theoretically explained by their finer grain size and more uniform phase distribution, which enhance the alloy's ability to accommodate plastic deformation by promoting uniform slip and reducing localized strain accumulation [34]. Moreover, rapid solidification during spray forming limits the formation of coarse intermetallics and minimizes micro segregation, both of which are detrimental to ductility. In contrast, the coarse, brittle intermetallic compounds (Al_3Ni, Al_3CuNi) formed in AC alloys (particularly with higher Ni content) have been reported to degrade elongation due to their tendency to fracture early and initiate cracks under tensile stress [35]. Similar trends of improved ductility through microstructure refinement have been documented in high-performance Al-Si-Cu-Ni piston alloys subjected to rapid solidification routes [33].

Table 15
Reduction in the yield strength of AC alloys with temperature.

Alloy	A1	A2	A3
Temperature (°C)	% Reduction	% Reduction	% Reduction
100°C	7.90 %	7.48 %	5.50 %
200°C	8.45 %	7.19 %	6.90 %
300°C	15.38 %	13.58 %	10.40 %

Table 16
Reduction in yield strength with temperature in SF alloys.

Alloy	S1	S2	S3
Temperature (°C)	% Reduction	% Reduction	% Reduction
100°C	5.05 %	4.64 %	2.01 %
200°C	6.47 %	5.43 %	2.05 %
300°C	10.60 %	6.89 %	3.70 %

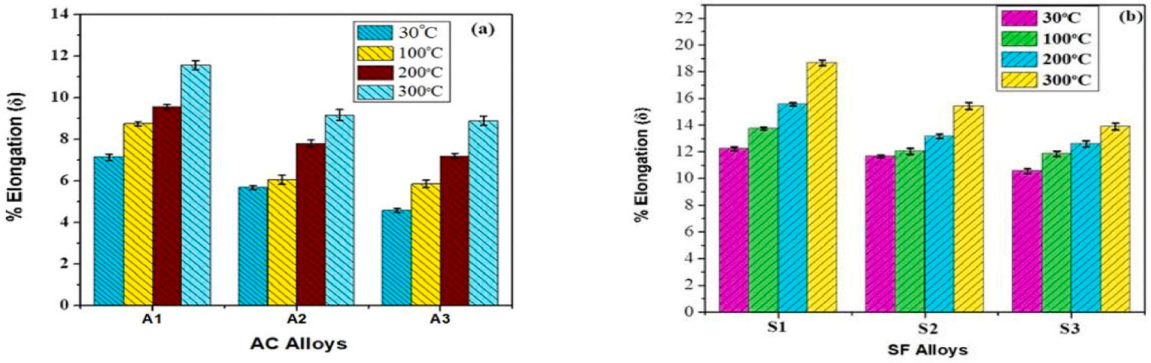

Fig. 11. Variation in the % elongation with temperature for **(a)** AC alloys; **(b)** SF alloys.

3.4.3. Morphology of fractured surfaces

The SEM fractured surface morphologies of the AC alloys at room temperature are shown in Fig. 12. The A1 alloy SEM fractography (Fig. 12(a)) is primarily composed of zones that are rather flat and featureless. This suggests that cracks may propagate during deformation at the Si/matrix interface as well as at the intermetallic/matrix interface, potentially leading to alloy failure. This behaviour is typical of interfacial decohesion seen in Al–Si alloys where stress concentration near rigid Si particles promotes crack initiation, especially in coarse-grained microstructures [36]. The Fig. 12(b) shows the A2 alloy fractograph. It mainly consists of more facets, and a few dimples between two and five microns in size are clearly visible in the fractograph, indicating that the micro voids connected quickly. Furthermore, a series of cracks were noted in the area surrounding the interface of the α-Al matrix and the intermetallic phase. Such mixed features of fracture, with both cleavage planes and ductile dimples are commonly reported in alloys containing Al_2Cu or Al_3Ni, as the sharp interface of these intermetallics can initiate decohesion during tensile loading [35].

The fractograph of the A3 alloy is shown in Fig. 12(c), where large facets are readily visible, indicating weak ductile fracture. The primary failure mode observed in the examined alloy was quasi-cleavage fracture. As the volume fraction of the Ni content increases, the proportion of cleavage planes also increases. The coarse primary Si phase that the cracks follow is close to the intermetallic and Al matrix, indicating that it is unlikely that the matrix will crack through the interfaces because of the weak phase connection. This fracture tendency has been corroborated in studies where higher Ni content resulted in brittle Al_3CuNi or Al_3Ni phases that reduce the alloy's overall plasticity [37].

The fractograph of the A1 alloy at 300°C (Fig. 13(a)) reveals the presence of numerous small voids and dimples, which are attributed to the fracture of Si and Si eutectic particles. The gradual fracturing of these particles in the plastic zone increases the overall crack propagation rate. The alloy fractograph has dimples in addition to cleavage planes. This observation implies that α-Al undergoes a particular degree of deformation before breaking, which is in line with the elongation percentage growth. This type of fracture transition with increasing temperature is consistent with thermally activated dislocation movement and matrix softening, which enhances ductile failure mechanism in Al alloys [38]. The A2 alloy fracture surface morphology (Fig. 13(b)) indicates a transition from brittle fracture to a combination of brittle and ductile fracture as the temperature increases. Small, ductile dimples with dispersed particles of the intermetallic phase are visible in Fig. 13 (b). The A3 alloy fracture surface (Fig. 13(c)) displays a mixed ductile trans-crystalline character, with deep dimples signifying extensive plastic deformation and typical ductile features. The Fig. 13(c) provides evidence of deboned Si particles and coarse intermetallic phase precipitates within the dimples, suggesting that the ductility of the alloy is improved at elevated temperatures. Such observations are in agreement with fracture studies of heat-resistant Al–Si–Cu–Ni alloys where elevated temperatures reduce interfacial stresses and activate more plastic deformation pathways in the matrix [39].

The Fig. 14 displays the SEM tensile fractograph of SF alloys tested at 30°C. The fractograph of S1 alloy, as shown in Fig. 14(a), has coexisting facets and underdeveloped pits. Nonetheless, the alloy exhibits a considerable amount of ductility and a reasonable ductile fracture.

The primary Si particles are linked to a few large dimples, small microscopic cracks and many micro voids that make up the fractured surface**.** This indicates that micro void coalescence and particle-matrix decohesion are active fracture mechanisms, typically observed in refined Al–Si systems where moderate intermetallics enable energy absorption through ductile tearing [40]. The S2 alloy fracture (Fig. 14(b)) displays tiny, poorly defined facets joined by shallow dimples or tear ridges within the facets. The facet center exhibits a minor river pattern extending outward. The presence of tear ridges and river patterns signifies a quasi-cleavage fracture mode, often occurring when intermetallics are more fragmented but still capable of initiating micro cracks under tensile loading [41]**.** The SEM fractograph of the S3 alloy is displayed in Fig. 14(c). It is made up of tiny micro voids and cracks connected to the principal Si and intermetallic phases. There are premature ductile dimples and microscopic voids on the fractured surface, indicating highly ductile fracture. Such morphology corresponds to improved toughness and plastic strain tolerance, attributed to the fine and uniform microstructure obtained by spray forming, which impedes crack propagation by distributing strain more evenly across the matrix [42]**.** SF alloys are stronger because of the homogenous dispersion and refinement of different components. This microstructural refinement leads to a Hall–Petch type strengthening and contributes to simultaneous enhancement of both strength and ductility, as reported in numerous studies on rapidly solidified Al-Si-Cu-Ni alloys [43,44].

The fractograph of the S1 alloy at 300°C is shown in Fig. 15(a). Large dimples formed and spread across the whole fractured surface of the alloy, which demonstrated a fully ductile fracture mode. Furthermore, at 300°C the dimples are even more enlarged than they are at 30°C (RT) and there are significantly more coalescent dimples and tear ridges on the fractured surface. The fractured morphology of S2 alloy at 300°C is shown in Fig. 15(b). It consists of a mixed mode of brittle and highly ductile fracture. Compared with those of the fractured surfaces at room temperature, the fractured surfaces of the SF alloys included much larger and wider dimples. The fractured morphology of S3 alloy depicted in Fig. 15(c) exhibit both dimples and cleavages, indicating a ductile fracture mode. Moreover, slip bands are observed in the cleavage facet, indicating plastic deformation in the second phase. The dimples in the SF alloys are smaller than those in the AC alloys, which aligns with the higher UTS. Compared to the S1 and S2 alloys, the S3 alloy has more dimples on the fractured surface, with deeper dimples, which is consistent with its greater elongation.

The reduced UTS and YS of the A1 alloy at 30°C are due to the presence of coarse primary Si particles in polyhedral and/or plate-like

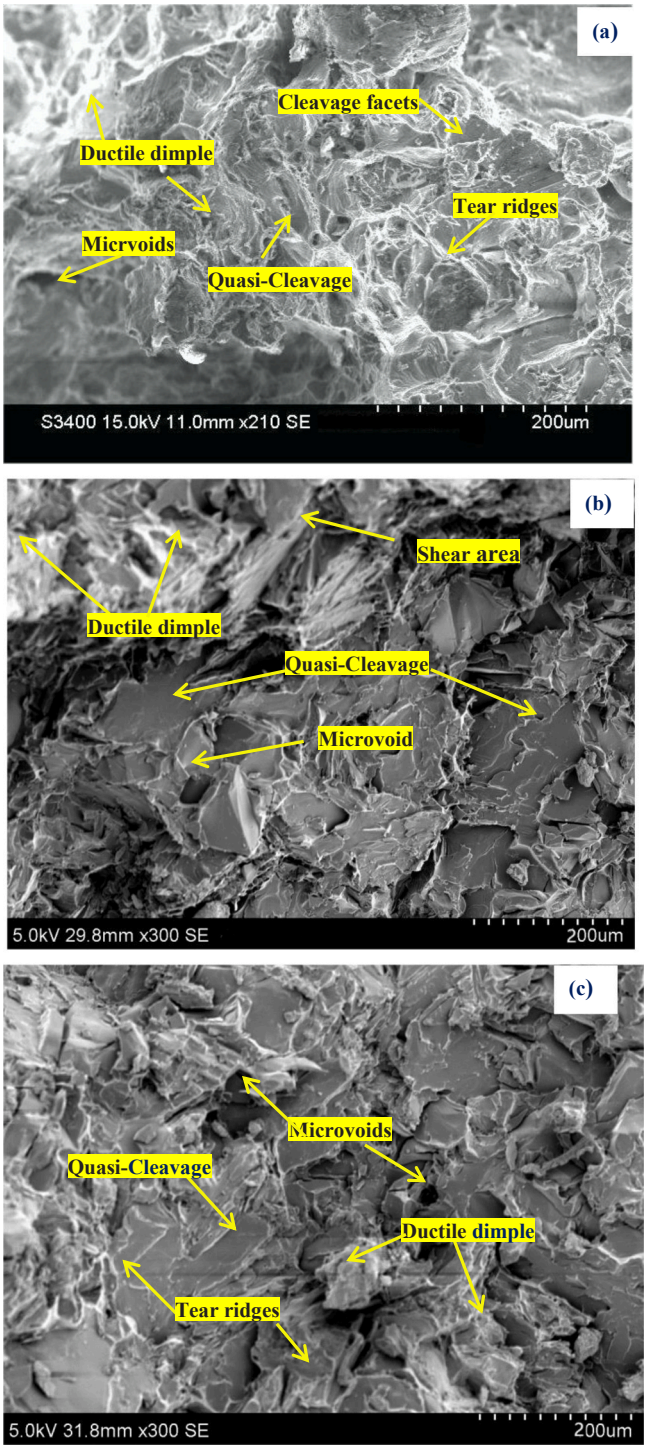

Fig. 12. Fractured surface morphology of AC **(a)** A1 **(b)** A2 and **(c)** A3 alloys at 30°C.

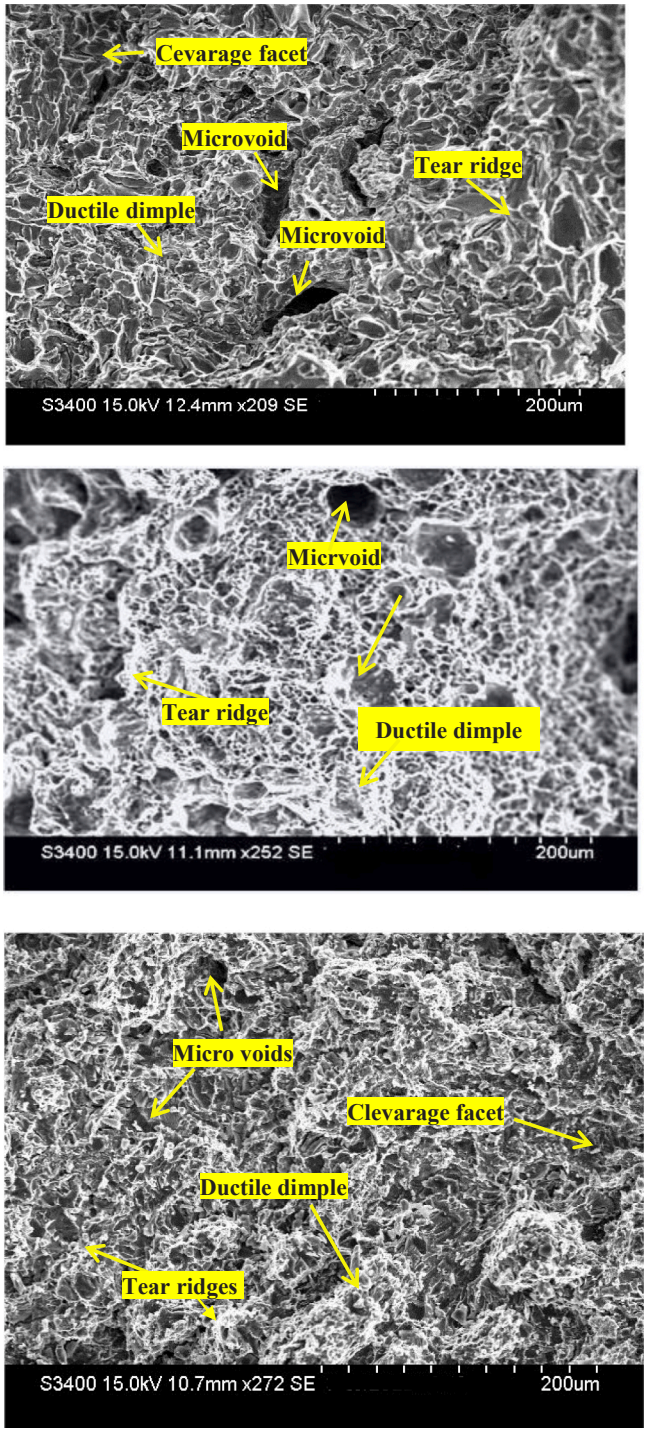

Fig. 13. Fractured surface morphology of AC **(a)** A1, **(b)** A2 and **(c)** A3 alloys at 300°C.

forms, as well as eutectic Si with poor plastic compatibility. The interface with the soft matrix experiences stress accumulation, leading to increased levels of strain. Brittleness increases with increasing Si content and the development of small cracks and voids when subjected to tensile stress [45]. The development of micro cracks and voids is due to plastic incompatibility between the ductile Al matrix and the Si particles present within the matrix. The addition of Cu and Ni to Al-15Si alloy often causes an increase in both the UTS and YS at 30°C (RT). The Cu and Ni dissolve in the aluminum matrix to a certain extent, creating a solid solution that impedes dislocation movement, thus increasing the UTS of the alloy. Additionally, the addition of Cu and Ni to Al-Si alloys results in the formation of hard intermetallic (Al_2Cu, Al_3CuNi and Al_3Ni) phases.

These phases act as obstacles to dislocation motion, significantly increasing the YS and UTS through precipitation hardening. The S1 alloy exhibits superior strength and ductility due to appropriate interface bonding, which is enabled by the even dispersion of fine primary Si particles in the Al matrix and the increased surface-to-volume ratio of Si particles. The improvement in the UTS of S1, S2 and S3 alloys is due to the refinement of the microstructure and the uniform distribution of primary Si particles and fine intermetallics. Furthermore, SF alloys do not possess connected brittle secondary phases and they can withstand a

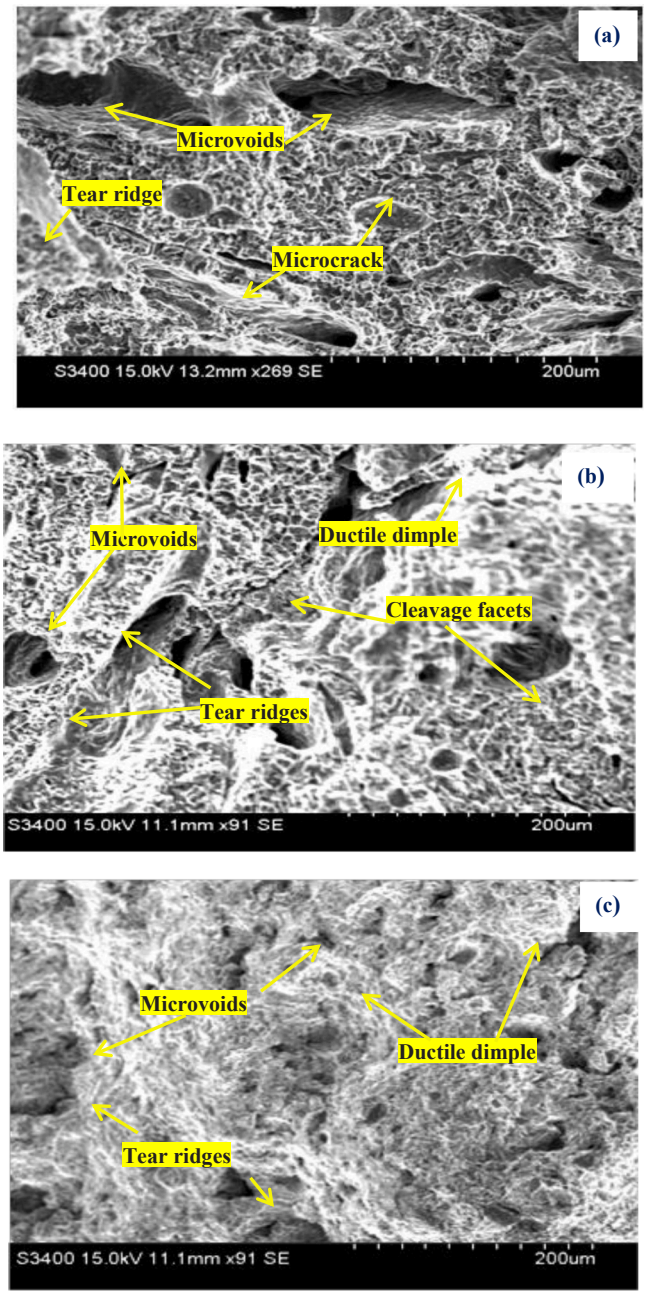

Fig. 14. Fractured surface morphology of SF **(a)** S1, **(b)** S2 and **(c)** S3 alloys at 30°C.

considerable amount of plastic deformation before fracture, resulting in improved ductility [46]. The coarse form of hard and brittle Si phases in hypereutectic Al—Si alloy consists of coarse primary material and has a limited plastic deformation ability even at elevated temperatures. Past research [47] revealed that the morphology and size of eutectic Si and intermetallics have little effect on the strain hardening of the alloy. The properties of α-Al substantially affect the deformation characteristics of AC alloys at elevated temperatures. According to previous studies, the UTS of a cast Al—Si piston alloy 'σ' can be described by the Eq. (3) [48]

$$\sigma = \left(1 - f_p\right)\sigma_m + f_p\sigma_p \tag{3}$$

where σ_m and σ_p are the fracture strengths of the α-Al and brittle phases respectively

and f_p. s the volume percentage of the phases

The softening of α-Al is the primary reason for the decrease in UTS as

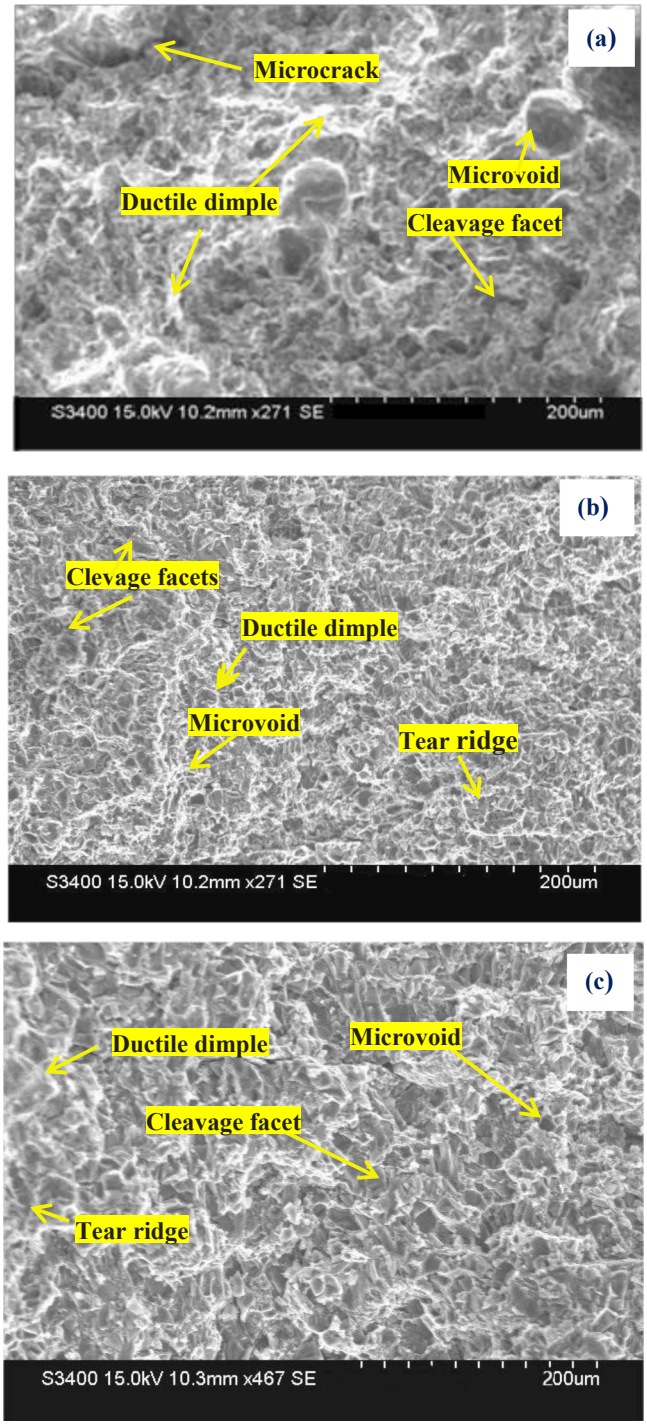

Fig. 15. Fractured surface morphology of SF **(a)** S1, **(b)** S2 and **(c)** S3 alloys at 300°C.

the brittle phases remain stable under the testing temperatures used in this study. The alloy strength decreases with temperature and is correlated with α-Al. At moderately elevated temperatures, some dislocation traces are detected in the samples at 100°C, indicates that α-Al experiences a mild and uniform deformation. This agrees with the significantly limited ductility exhibited under these thermal conditions. A noticeable increase in dislocation density along with the formation of entangled dislocation structures after tensile testing at 200°C, indicates that the α-Al phase has experienced significant plastic deformation. Sub grains form during tension at 300°C, indicates that α-Al has better ductility during tension above 300°C. This leads to a significant increase in

elongation. The discussion above leads to the conclusion that the deformation behavior of α-Al is similar to that of the whole alloy. The SF alloys have higher YS and UTS than those produced by conventional casting. The increase in UTS and decrease in ductility with increasing amount of Ni in the Al-15Si alloy can be attributed to the increasing volume fraction of the intermetallic Al_2Cu, Al_3CuNi and Al_3Ni phases. The cavitation resistance is reduced when intermetallic phases that are plastically incompatible are present in the matrix, resulting in the occurrence of early micro cracking and consequently reducing ductility when subjected to tensile loads. Compared with AC alloys, SF alloys have better ductility. This is because they do not have brittle secondary phases and can resist significant plastic deformation before fracturing [49]. The low ductility of AC alloys is caused by cracking at the interfaces of the Si/Al matrix. The hypereutectic Al-Si alloy has polyhedral primary Si and needle-shaped eutectic Si particles, which are not plastically compatible and create stress when in contact with the ductile Al matrix. A high Si content in an alloy causes the development and advancement of micro voids and micro cracks under tensile strain, leading to a low UTS. Furthermore, defects found in AC alloys decrease the area that can withstand stress, weakening the alloy and reducing the maximum amount of stress it can carry. Compared to SF alloys, the AC alloys exhibited lower UTS, YS and ductility.

4. Conclusions

In the present study, the effect of Ni and Cu on the mechanical properties of spray formed Al-15Si alloys at room and elevated temperatures was explored and the following conclusions may be drawn.

- The microstructures of S1, S2 and S3 alloys show the presence of fine spherical shaped primary Si and eutectic Si phases and fine Ni-rich and Cu-rich intermetallic particles uniformly dispersed in the Al matrix.
- The cast alloys consisted of primary coarse Si, a flake type eutectic phase, a Cu-rich intermetallic phase in the form of Chinese-script and a network of short strips and are dispersed non uniformly in dendritic Al matrix.
- The SF alloys exhibited higher hardness than the AC alloys at all temperatures, with a maximum increase of 74 % at room temperature. The study suggested that the evenly dispersed thermally stable intermetallic phases, such as Al_3Ni and Al_3CuNi contributed to the improved hardness and thermal stability of the SF alloys.
- SF alloys demonstrated a significant increase in UTS by 25 % at 30°C (RT) and 40 % at 300°C, as compared to that of AC alloys, indicating their superior strength and thermal stability.
- The yield strength (YS) of the SF alloys is higher than that of the AC alloys at all temperatures, with a minimal decrease in the YS (2–14.65 %) at 300°C.
- The SF alloys exhibit superior elongation properties, with a progressive increase in % elongation with temperature. The S1 alloy shows the greatest increase (14.3–18.6 %), and the S3 alloy shows the lowest increase (10.5–14 %) between 30°C and 300°C.
- The addition of Cu and Ni to Al-15Si alloys improved the strength, elongation properties & thermal stability of the alloys, making them the promising materials for high-temperature applications.

Abbreviations

The following abbreviations are used in this manuscript:

AC, As-cast; SF, Spray formed; RT, Room temperature; UTS, Ultimate tensile strength; YS, Yield strength; SEM, Scanning electron microscopy; EDS, Energy Dispersive X-ray Spectroscopy

CRediT authorship contribution statement

Alavandi Mehabubsubahani R: Writing – review & editing, Writing – original draft, Visualization, Validation, Methodology, Investigation, Formal analysis, Data curation. **Goudar Dayanand M:** Writing – review & editing, Writing – original draft, Visualization, Validation, Supervision, Methodology, Investigation, Formal analysis, Conceptualization. **Subraya Krishna Bhat:** Writing – review & editing, Visualization, Methodology. **Kurahatti Rajashekar V:** Writing – review & editing, Visualization, Resources, Methodology, Investigation. **Raghukumar Bommenahalli:** Writing – review & editing, Visualization, Validation. **K Raju:** Writing – review & editing, Writing – original draft, Visualization, Validation, Supervision, Methodology, Conceptualization. **Pinto Deesy G:** Writing – review & editing, Visualization, Validation.

Funding

This research received no external funding.

Declaration of Competing Interest

The authors declare that they have no known competing financial interests or personal relationships that could have appeared to influence the work reported in this paper.

Data availability

The data presented in this study are available within the article.

References

[1] L. Gao, Y. Zhang, H. Li, J. Wang, X. Chen, Research on the mechanical properties and microstructural evolution of Al–Si alloy for automotive rear floors based on simulation-assisted casting, Materials 18 (9) (2025) 2143, https://doi.org/10.3390/ma18092143.
[2] M.R. Alavandi, J. Haider, D.M. Goudar, Investigation of the influence of ni and cu additions on the wear behavior of spray formed Al-15Si alloy at elevated temperature, Silicon 15 (2023) 5963–5980, https://doi.org/10.1007/s12633-023-02465-9.
[3] Love Kerni, Ankush raina; mir irfan ul haq. Performance evaluation of aluminum alloys for piston and cylinder applications, Mater. Today. Proc. 5 (90) (2018) 18170–18175.
[4] H. Zhang, Q. Liu, Y. Wang, X. Zhang, Precipitation behavior and strengthening mechanisms of cu and mg in Al–Si casting alloys for automotive applications, J. Mater. Res. Technol. 28 (2024) 3312–3323, https://doi.org/10.1016/j.jmrt.2024.03.112.
[5] Y. Chen, Z. Wang, J. Luo, *effect of cu content on microstructure and mechanical* properties of Al–Si–Cu alloys for automotive applications, J. Alloy. Compd. 944 (2024) 169293, https://doi.org/10.1016/j.jallcom.2023.169293.
[6] J. Li, D. Wang, S. Chen, Y. Liu, Solidification behavior and intermetallic phase evolution in multi-component Al–Si casting alloys, Mater. Charact. 206 (2024) 112964, https://doi.org/10.1016/j.matchar.2024.112964.
[7] Hesham Elzanaty, Mechanical properties of Al-Si-Cu alloys at various temperatures, J. Mater. Sci. 49 (15) (2014) 5330–5340.
[8] E. Gariboldi, Microstructure and mechanical properties of hypo-and near- eutectic Al-Si-Cu alloys, J. Alloy. Compd. 767 (2018) 1238–1248.
[9] Y. Zhou, Q. Liu, W. Wu, J. Zhang, Effect of ni and cu additions on the microstructure and high-temperature mechanical properties of hypereutectic Al–Si alloys, J. Alloy. Compd. 957 (2024) 170696, https://doi.org/10.1016/j.jallcom.2023.170696.
[10] L. Liu, B. Qi, F. Xie, Y. Zhang, C. Zhu, Effects of fe and ni on the microstructure and high-temperature tensile properties of Al–Si aluminium alloys, J. Phys. Conf. Ser. 2510 (1) (2023) 012003, https://doi.org/10.1088/1742-6596/2510/1/012003.
[11] Z. Zhang, M.X. Zhang, Formation of Al3Ni phase in Al–Ni alloys under different solidification conditions, Intermetallics 19 (7) (2011) 1020–1026.
[12] H. Chen, S. Wu, J. Li, D. Zhao, S. Lü, Effects of low nickel content on microstructure and high-temperature mechanical properties of Al-7Si-1.5Cu-0.4Mg aluminum alloy, Metals 14 (2) (2024) 223, https://doi.org/10.3390/met14020223.
[13] Y. Chen, J. Liu, H. Wu, Effects of cu and ni additions on microstructure evolution and high-temperature mechanical properties of Al–Si alloys, J. Alloy. Compd. 956 (2024) 170512, https://doi.org/10.1016/j.jallcom.2023.170512.
[14] B.D. Cullity, S.R. Stock. Elements of X-ray Diffraction, 3rd ed., Prentice Hall, 2001.
[15] R. Kumar, R.P. Saini, A. Sharma, Microstructural characterization and XRD analysis of modified Al–Si alloys: effect of grain refinement and thermal processing, Mater. Today. Proc. 84 (2024) 1137–1143, https://doi.org/10.1016/j.matpr.2023.10.154.
[16] T. Zhang, X. Li, Y. Sun, Q. Wang, Effect of rapid solidification on microstructure and texture evolution of Al–Si based alloys: a comparative XRD study, Mater. Charact. 210 (2024) 112965, https://doi.org/10.1016/j.matchar.2023.112965.

[17] Li Yunguo, Yang Yang, Wu Yuying, Wang Liyan, Liu Xiangfa, Quantitative comparison of three Ni-containing phases to the elevated-temperature properties of Al–Si piston alloys, Materials Science Engineering A 527 (26) (2010) 71327137, https://doi.org/10.1016/j.msea.2010.07.073.
[18] Zhang Yun, Li Ruiqing, Chen Pinghu, Li Xiaoqian, Liu Zhilin, Microstructural evolution of Al2Cu phase and mechanical properties of the large-scale al alloy components under different consecutive manufacturing processes, J. Alloy. Compd. (2019), https://doi.org/10.1016/j.jallcom.2019.07.346.
[19] Zhou, W., Liang, Y., Zhang, S., & Gao, M. (2025). First-principles investigation of exceptional coarsening-resistant V-Sc (Al_2Cu)$_4$ nanoprecipitates in Al–Cu–Mg–Ag–Sc alloys. arXiv preprint. ⟨https://arxiv.org/abs/2502.17740⟩.
[20] X.L. Wan, L. Liu, D.Q. Zhao, Z.D. Wang, W.H. Wang, Grain refinement and nucleation behavior of Al_3Ni in aluminum alloys, J. Alloy. Compd. 457 (1–2) (2008) 138–142, https://doi.org/10.1016/j.jallcom.2007.03.090.
[21] H. Li, D. Zhao, Y. Liu, Q. Wang, Effect of ni on microstructure evolution and mechanical properties of Al–Si–Cu–Ni piston alloys, J. Mater. Sci. Technol. 110 (2022) 182–193, https://doi.org/10.1016/j.jmst.2021.05.064.
[22] W. Jiang, H. Hu, Effect of ni content on the microstructure and wear properties of Al–Si–Cu–Ni–Mg piston alloy, Mater. Charact. 59 (10) (2008) 1367–1372.
[23] M.S. Reddy, P.S. Reddy, Investigation on nickel modified hypereutectic Al–Si alloys for high temperature applications, Mater. Today. Proc. 46 (2021) 5147–5153.
[24] L. Zhang, S. Wu, Phase evolution in Al–Si–Cu–Ni piston alloys during solidification and heat treatment, J. Alloy. Compd. 479 (1–2) (2009) 719–723.
[25] M. Song, et al., Microstructural evolution and mechanical properties of Al–Si–Cu–Ni–Mg alloys with high nickel content, Mater. Sci. Eng. A 413–414 (2005) 204–209.
[26] Bin Yang, Feng Wang, J.S. Zhang, Microstructural characterization of in situ TiC/Al and TiC/Al–20Si–5Fe–3Cu–1Mg composites prepared by spray deposition, Acta Mater. 51 (17) (2003) 4977–4989.
[27] D.J. Dunstan, A.J. Bushby, Grain size dependence of the strength of metals: the Hall–Petch effect does not scale as the inverse square root of grain size, Int. J. Plast. 53 (2014) 56–65, https://doi.org/10.1016/j.ijplas.2013.07.004.
[28] D. Zhao, H. Li, Y. Liu, Q. Wang, Microstructural stability and high-temperature performance of Ni- and Cu-containing intermetallics in Al–Si piston alloys, J. Mater. Sci. Technol. 85 (2021) 1–10, https://doi.org/10.1016/j.jmst.2021.01.018.
[29] X. Zhao, J. Dong, M. Li, Z. Ma, Microstructural evolution and tensile properties of Al–Si piston alloys during long-term thermal exposure, Metals 14 (5) (2024) 535.
[30] A. Munitz, C. Cotler, G. Kohn, A. Landau, Influence of rapid solidification on the microstructure and mechanical properties of Al–Si–Cu alloys, Mater. Sci. Eng. A 660 (2016) 183–195, https://doi.org/10.1016/j.msea.2016.02.010.
[31] Hector Torres, Varga Markus, M. Rodríguez Ripoll, High temperature hardness of steels and iron-based alloys, Mater. Sci. Eng. A 671 (2016) 170–181, https://doi.org/10.1016/j.msea.2016.06.058.
[32] Akbari, M. Karbalaei, H.R. Baharvandi, K. Shirvanimoghaddam, Tensile and fracture behavior of nano/micro TiB2 particle reinforced casting A356 aluminum alloy composites, Mater. Des. 66 (2015) 150–161, https://doi.org/10.1016/j.matdes.2014.10.048.
[33] Q. Yu, J. Zhao, Z. Fan, Microstructure evolution and high-temperature mechanical properties of Al–Si–Cu–Ni alloy, Mater. Des. 60 (2014) 213–220.
[34] Y. Wang, Y. Zhang, J. Wu, H. Wang, Influence of spray forming on the microstructure and mechanical properties of Al–Si–Cu alloys, Mater. Sci. Eng. A 867 (2023) 145050, https://doi.org/10.1016/j.msea.2023.145050.
[35] Z. Liu, Y. Han, B. Sun, Influence of ni content on microstructure and mechanical properties of Al–Si–Cu piston alloys, Mater. Sci. Eng. A 527 (7–8) (2010) 1986–1992.
[36] J. Wang, A. Ma, Fracture behavior of Al–Si–Cu alloys: effect of intermetallics and si morphology, Mater. Sci. Eng. A 609 (2014) 82–88.
[37] J. Zhang, X.G. Chen, Y.C. Lin, Effect of ni content on fracture and tensile behavior of Al–Si–Cu–Ni–Mg alloys, Metall. Mater. Trans. A 46 (4) (2015) 1732–1744.
[38] S. Kumar, R. Shabadi, B.S. Murty, High-temperature deformation and fracture behavior of Al–Si alloys: influence of temperature and strain rate, Mater. Sci. Eng. A 608 (2014) 1–9, https://doi.org/10.1016/j.msea.2014.04.022.
[39] Q. Yu, J. Zhao, Z. Fan, High-temperature mechanical properties and fracture behavior of Al–Si–Cu–Ni piston alloys, Mater. Sci. Eng. A 604 (2014) 1–8.
[40] S. Kumar, Y.V.R.K. Prasad, Deformation and fracture behavior of Al–Si alloys with refined primary si and intermetallic phases, Mater. Des. 29 (7) (2008) 1301–1306.
[41] H. Li, et al., Influence of ni addition on microstructure and fracture characteristics of Al–Si piston alloys, J. Alloy. Compd. 512 (1) (2012) 63–69.
[42] M.T. Sijo, R. Jayaganthan, Microstructural evolution and tensile properties of spray formed Al–Si–Cu alloys, Mater. Sci. Forum 879 (2017) 2254–2259.
[43] C. Lin, et al., Influence of spray forming on the mechanical properties and fracture behavior of Al–Si–Cu–Ni alloys, Mater. Charact. 81 (2013) 98–106.
[44] H. Lu, et al., High-performance Al–Si alloys via rapid solidification: strengthening mechanisms and fracture behavior, Acta Mater. 110 (2016) 190–200.
[45] L. Lu, A.K. Dahle, D.H. StJohn, The effect of combined modification and grain refinement on the microstructure and mechanical properties of hypoeutectic and eutectic Al–Si foundry alloys, Mater. Sci. Eng. A 390 (1–2) (2005) 106–115, https://doi.org/10.1016/j.msea.2004.08.017.
[46] S.H. Khaji, D.M. Goudar, J. Haider, K. Raju, Microstructural features and mechanical properties of spray -formed hypereutectic Al-Si-Ti alloy, Adv. Mater. Process. Technol. 11 (2) (2024) 1018–1035, https://doi.org/10.1080/2374068X.2024.2342621.
[47] Xiang Su, Yuan Lei Hongjie Qu, Yuede Cao Rui Hou, Zhixiang Qi Suniya Siddique, Xueyi Fan Guoyan Shen, Influence of ni on the microstructures and mechanical properties of Heat-Treated Al-Cu-Ce-Mn-Zr alloys, Crystals 13 (3) (2023) 380, https://doi.org/10.3390/cryst13030380.
[48] W.O. Soboyejo, "9.3.1 Constant-Strain and Constant-Stress rules of mixtures". Mechanical properties of engineered materials, Marcel Dekker, 2003. ISBN 0-8247-8900-8. OCLC 300921090.
[49] Y. Zhou, H. Zhang, X. Li, J. Liu, Microstructural evolution and tensile behavior of spray-formed hypereutectic Al–Si alloys, Mater. Sci. Technol. 40 (3) (2024) 205–215, https://doi.org/10.1080/2374068X.2024.2342621.